J. Mech. Phys. Solids 156 (2021) 104610

Contents lists available at ScienceDirect

Journal of the Mechanics and Physics of Solids

journal homepage: www.elsevier.com/locate/jmps

Achieving enhanced adhesion through optimal stress distributions

Aoyi Luo, Kevin T. Turner *

Department of Mechanical Engineering and Applied Mechanics, University of Pennsylvania, Philadelphia, PA 19104-6315, USA

ARTICLE INFO

Keywords:
Adhesion
Interface failure
Optimization
Dry adhesive

ABSTRACT

Dry adhesives that rely on surface force mediated adhesion, such as van der Waals forces, are important in applications ranging from robotics to manufacturing. The maximum theoretical adhesion strength of a contact is achieved when the stress is uniformly distributed over the entire contact area as the full potential of all the bonds at the interface is realized in this scenario. Most dry adhesive structures are composed of a tip layer that forms contact and a support structure that transfers load from the far field to this tip structure. Here, we determine the displacement distribution that must be applied on the tip layer to generate an optimum interfacial stress distribution. We realize this through a linear, closed-form optimization framework that uses data obtained from finite element analysis for a few basis cases. It was found that adhesion can be maximized by applying an optimum displacement on the tip layer that consists of uniform tension in the center, a peak tension between the center and the edge, and compression near the edge. The displacement applied on the tip layer of a mushroom-shaped, composite, and novel segmented composite structures are then analyzed and compared with the optimal case to guide the design of dry adhesives.

1. Introduction

Structures that provide reversible adhesion to a broad range of substrates via relatively weak surface forces have received significant interest in recent years because of the unique functionality they provide (Del Campo et al., 2007; Hensel et al., 2018; Murphy et al., 2009). Rather than relying on specific bonding via chemistry, these "dry adhesives" exploit structures with engineered geometries that enable strong adhesion to be realized despite the relatively weak nature of surface force interactions such as van der Waals forces. The versatility, reusability, and repeatability of dry adhesives have led to their use in a broad range of applications, including reusable tapes (Bartlett et al., 2012; Kim and Sitti, 2006; King et al., 2014), wearable devices (Drotlef et al., 2017), climbing robots (Aksak et al., 2008; Menon et al., 2004; Pope et al., 2017), robotic gripping (Hawkes et al., 2018; Song et al., 2017; Song and Sitti, 2014; Zhou et al., 2013), and microtransfer printing (Carlson et al., 2012; Kim-Lee et al., 2014; Meitl et al., 2006).

The maximum theoretical adhesion strength of a contact is achieved when the stress is uniformly distributed over the entire contact area as the full potential of all the bonds at the interface is realized in this scenario. However, when a load is applied to an adhered interface between two dissimilar materials or two bodies with different geometries, there is almost always a stress concentration near the edge of the contact that leads to a highly nonuniform stress distribution. The high, localized stress at the edge facilitates crack initiation at the interface and results in an effective adhesion strength that is far less than the theoretical maximum (Khaderi et al., 2015). Several strategies have been examined to mitigate the effect of this stress concentration and to realize a more uniform stress

* Corresponding author.
E-mail address: kturner@seas.upenn.edu (K.T. Turner).

https://doi.org/10.1016/j.jmps.2021.104610
Received 26 February 2021; Received in revised form 4 August 2021; Accepted 10 August 2021
Available online 12 August 2021

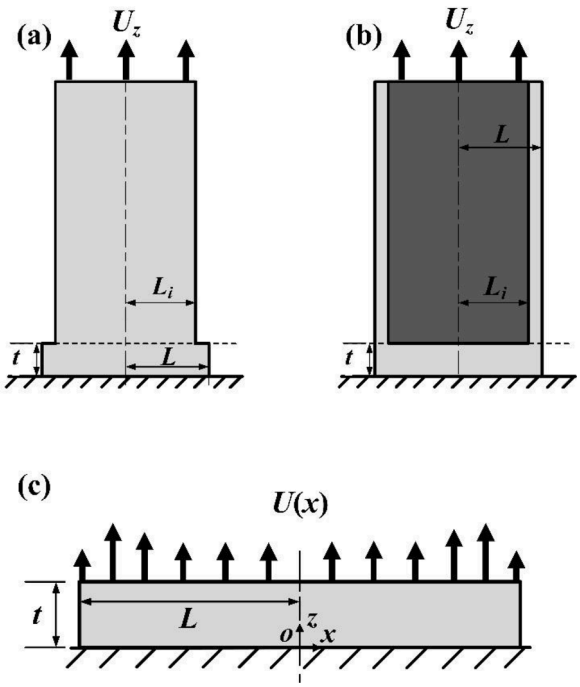

Fig. 1. (a) Schematic of a mushroom-shaped adhesive structure. (b) Schematic of a composite adhesive structure (the dark gray region is stiffer than the light gray region). (c) Schematic of a flat layer adhered to a flat substrate with a displacement, $U(x)$, applied on its top surface (plane strain).

distribution in order to approach the optimal case. Gao and Yao (2004) identified the optimum tip shape for a single fiber in a fibrillar adhesive to realize a uniform stress distribution at the point of pull-off. Their work provided a novel unique strategy to improve adhesion strength, but the approach is difficult to implement in practice because it is highly sensitive to small variations in the tip shape. Moreover, the optimum tip shape is different for different materials and depends on the elastic modulus and theoretical adhesion strength of the material. A challenge with this approach is that the value of the theoretical adhesion strength for a given material pair is typically not known. Beyond tip shape, Gao and Yao (2004) and Gao et al. (2005) demonstrated that a uniform stress distribution can be achieved irrespective of the shape of the contacting bodies when the size of the contact is smaller than a critical length scale, which is on the order of 100 nm for typical materials used in dry adhesives. This approach provides another route to maximize adhesion strength, but the fabrication of sub-μm size adhesive structures over large areas is challenging.

Although a perfectly uniform stress distribution at the interface is difficult to achieve, multiple dry adhesive designs have been developed to generate a favorable interfacial stress distribution that results in enhanced adhesion strength. A mushroom-shaped fiber that mimics the spatula-shaped tips of the setae on geckos' feet, as shown in Fig. 1(a), leads to a stress distribution in which the stress is elevated in the center of the contact and the stress concentration near the edge is reduced (Aksak et al., 2014; Balijepalli et al., 2016; Carbone et al., 2011; Kim et al., 2020). Mushroom-shaped fibers have been experimentally demonstrated to have high adhesion strength relative to cylindrical fibers on both the micrometer (Hensel et al., 2018; Kim et al., 2012) and millimeter (Gorb and Varenberg, 2007) scales. Similarly, a composite fiber with a stiff core and compliant shell (Fig. 1(b)) also has a reduced stress concentration near the edge of the contact and thus has enhanced adhesion compared to a homogenous fiber (Balijepalli et al., 2017; Fischer et al., 2017; Minsky and Turner, 2017, 2015; Tatari et al., 2018).

There has been extensive work to improve the adhesion strength of dry adhesives by optimizing the design of mushroom-shaped and composite fibrillar structures. Most of these studies have done this through parametric studies in which finite element analysis is used to explore a prescribed parametric space (Aksak et al., 2014; Balijepalli et al., 2017, 2016; Benvidi and Bacca, 2021; Carbone and Pierro, 2012; Minsky and Turner, 2017, 2015; Zhang et al., 2021). Recently, deep learning techniques have also been applied to optimize the shape of fibers with flared ends by using 2×10^5 finite element simulations to train a neural network and then using this trained network to search through an extensive design space (Kim et al., 2020). Though mushroom-shaped and composite fibrillar structures have been studied extensively, they are neither the only nor the optimum dry adhesive design that can lead to a favorable interface stress distribution that results in enhanced adhesion.

The design of a single fiber in a fibrillar dry adhesive or adhesive stamp for a process such as microtransfer printing (Carlson et al., 2011; Luo and Turner, 2020; Sen et al., 2018), including mushroom-shaped and composite structures, can be decomposed into two sections as shown in Fig. 1(a) and (b). First, there is a tip layer that has sufficient smoothness and compliance to achieve conformal contact with another surface. Second, there is a support structure above the tip layer that transfers loads to the tip layer and applies a specific displacement (or corresponding traction) boundary condition on the top of the tip layer. Although various shapes of the tip (e.g. flat, spherical) have been studied, a flat tip that makes contact over its entire projected area has been the predominant shape used as

it results in higher contact areas and higher adhesion strengths than other shapes (Micciché et al., 2014; Tan et al., 2020; Tang et al., 2005). For a fixed tip geometry, the ability to modify the interfacial stress distribution lies in the design of the support structure above the tip layer (Aksak et al., 2011; Bacca et al., 2016; Khungura and Bacca, 2021; Kim et al., 2007; Long et al., 2008). A support structure that transfers load in a manner that results in a low stress concentration and a uniform stress distribution at the interface will lead to higher effective adhesion strength. Recent developments in compliant mechanisms and architected materials have demonstrated the ability to design structures that have prescribed mechanical responses (Howell et al., 2013; Surjadi et al., 2019; Yu et al., 2018). Moreover, techniques like 3D printing and two-photon lithography have enabled fabrication of more complex and precise structures (Anscombe, 2010; Salonitis, 2014; Thiel and Hermatschweiler, 2011). The advances in these fields provide the opportunity to realize adhesives with support structures that generate a prescribed displacement boundary condition on the top of the tip layer to produce a near optimal stress distribution at the interface. To design such a support structure, one must first determine the displacement boundary condition on the top surface of the tip layer that will generate an optimal stress distribution at the interface.

We present an optimization framework to find the *practical optimum displacement boundary condition* on the top surface of a flat elastic tip layer that yields an interfacial stress distribution with: (1) the minimum deviation from a uniform stress distribution, and (2) no tensile stress concentration at the edge. This is determined under the assumptions of linear elasticity and the displacement boundary condition is *practical* because it is determined subject to the constraint that the strains are within the elastic limit of the tip material. Different from many of the previous optimization studies, the optimization framework here is solved in a linear closed form using data obtained from finite element analysis for a few basis cases.

2. Analysis framework

The analysis in this paper examines the design of adhesive structures by considering the stress distribution at the interface and analysis of the stress singularity at the edge, with assumptions that are consistent with linear elastic fracture mechanics (LEFM). Similar assumptions and approaches have been widely used to analyze dry adhesives (Balijepalli et al., 2017, 2016; Benvidi and Bacca, 2021; Khaderi et al., 2015; Minsky and Turner, 2017, 2015). We consider a thin elastic layer in 2D (plane strain) with half width L and thickness t adhered to a rigid substrate and subjected to a prescribed displacement on the top surface (Fig. 1(c)). By symmetry, the region $0 < x < L$ is analyzed and a symmetry boundary condition is assumed at $x = 0$. The layer is traction free at $x = L$. The elastic layer is adhered to a rigid flat substrate at $z = 0$ and no-slip is assumed at this interface. A displacement, $U(x)$, is applied at $z = t$. The layer is assumed to be homogenous, linear elastic, isotropic, and nearly incompressible with a Poisson's ratio $\nu = 0.49$, which is representative of many elastomers used in dry adhesives. This leads to dundurs parameters $\alpha = -1$, $\beta \approx 0$ at the interface (Hutchinson and Suo, 1991). The results are presented in nondimensional form and are independent of the value of the modulus E. All the configurations and structures studied in this paper are assumed to be in plane strain unless otherwise stated (we present results for axisymmetric cases with the same boundary conditions and elastic properties as the plane strain cases in Appendices B and G).

The normal stress distribution at the interface, $\sigma_{zz}/\sigma_{zz\text{-}avg}$ ($\sigma_{zz\text{-}avg}$ is the average normal stress) is critical in determining the effective adhesion strength of an interface (Gao et al., 2005; Gao and Yao, 2004). The effective adhesion strength is maximized when the deviation of the normal stress from the average normal stress is minimized and the tensile stress singularity at the edge is suppressed. The goal of the optimization study is to determine the prescribed displacement $U(x)$ that minimizes the stress non-uniformity and edge singularity subject to the constraint the $U(x)$ does not introduce strains that exceed the elastic limit of the layer.

2.1. Linear superposition

Shear displacements on the top surface of the tip layer only have a small effect on the normal stress distribution at the interface, thus we assume the shear displacement to be zero and focus on the case where only normal displacement is applied on the top surface of the tip layer. Assuming $U(x)$ is continuous and differentiable at $x > 0$, it can be expressed as a polynomial series. Keeping polynomials up to order n, the components of $U(x)$ can be expressed as:

$$\begin{aligned} U_z\left(\frac{x}{L}\right) &= \sum_{i=0}^{n} a_i \cdot \delta_z^i\left(\frac{x}{L}\right) \\ U_x\left(\frac{x}{L}\right) &= 0 \end{aligned} \tag{1}$$

where U_z and U_x are the normal and shear components of $U(x)$, respectively. $\delta_z{}^i$ is the polynomial basis of order i ($0 \le i \le n$) (e.g., $\delta_z{}^0 = 0.095(\sigma_{zz\text{-}avg}t/E^*)$, $\delta_z{}^1 = 0.22(\sigma_{zz\text{-}avg}t/E^*)(x/L)$, $\delta_z{}^2 = 0.38(\sigma_{i,avg}t/E^*)(x/L)^2$ for $t/L = 0.1$, where $E^* = E/(1\text{-}\nu^2)$) and a_i is a coefficient ($0 \le i \le n$). As a higher order polynomial basis has a higher maximum magnitude of displacement (e.g., $\delta_z{}^0{}_{max} = 0.095(\sigma_{zz\text{-}avg}t/E^*)$, $\delta_z{}^1{}_{max} = 0.22(\sigma_{zz\text{-}avg}t/E^*)$, $\delta_z{}^2{}_{max} = 0.38(\sigma_{i,avg}t/E^*)$ for $t/L = 0.1$), we do not include higher order polynomials (e.g. $n > 10$ for $t/L = 0.1$) that will lead to an optimal $U(x)$ that exceeds the elastic limit of the tip layer (as shown later in Fig. 3). Polynomials are used in this paper not only because they are a commonly used basis function, but also because: (1) a higher-order polynomial basis function has a higher maximum magnitude of displacement as the above examples show, which allows us to limit the displacements (i.e. to avoid physically unreasonable solutions) by cutting off higher order polynomials; (2) We expect the pattern of the optimal displacement applied on the top surface of the tip layer to be a relatively uniform tension in the center and a region of concentrated displacement variation near the edge, and a polynomial basis is a basis that allows sharp variation near the edge as its gradient increases as x increases (for $n > 1$). Assuming linear elasticity, the principle of linear superposition allows the stress distribution at the adhered interface to be expressed as

a summation of the stresses generated by each δ_z^i:

$$\sigma_{zz}\left(\frac{x}{L}\right) = \sum_{i=0}^{n} a_i \cdot \sigma_z^i\left(\frac{x}{L}\right)$$
$$\sigma_{xz}\left(\frac{x}{L}\right) = \sum_{i=0}^{n} a_i \cdot \tau_z^i\left(\frac{x}{L}\right) \tag{2}$$

where σ_{zz} and σ_{xz} are the normal and shear stresses at the interface generated by displacements U_z. $\sigma_z{}^i$ and $\tau_z{}^i$ are the normal and shear stress distributions generated by normal displacement $\delta_z{}^i$. Finite element (FE) analysis was performed to find the normal stress distribution ($\sigma_z{}^i$) and shear stress distribution ($\tau_z{}^i$) generated by each polynomial basis ($\delta_z{}^i$).

For the configuration shown in Fig. 1(c), a stress concentration in the form of a stress singularity is present near the edge and this facilitates crack initiation and reduces the effective adhesion strength (Akisanya and Fleck, 1997; Balijepalli et al., 2017; Khaderi et al., 2015). For a nearly incompressible material, the stress within the stress singularity dominated region near the edge is (Balijepalli et al., 2017; Khaderi et al., 2015):

$$\begin{aligned} \sigma_{zz} &= H(L-x)^{-0.41} \\ \sigma_{rz} &= -0.51H(L-x)^{-0.41} \end{aligned} \tag{3}$$

where H is the magnitude of stress singularity. Eq. (2) holds within the stress singularity dominated region and substitution of Eq. (3) into Eq. (2) gives the overall magnitude of the stress singularity as a linear summation of the magnitudes of the stress singularities resulting from $\delta_z{}^i$:

$$H = \sum_{i=0}^{n} a_i \cdot H_z^i \tag{4}$$

where $H_z{}^i$ is the magnitude of the stress singularity generated by normal displacement $\delta_z{}^i$.

The stress distribution for each of the polynomial bases is obtained from FE. The overall stress distribution at the adhered interface for an arbitrary displacement given by Eq. (1) can be calculated from Eq. (2). It is convenient to have $\sigma_{zz\text{-}avg} = 1$ in the analysis, thus all the polynomial bases ($\delta_z{}^i$) are chosen in normalized forms such that the average normal stress generated by each basis is 1 (i.e. the average of $\sigma_z{}^i$ is 1). The average of σ_{zz} given by Eq. (2) with $\sigma_{zz\text{-}avg} = 1$ yields:

$$\sum_{i=0}^{n} a_i = 1 \tag{5}$$

2.2. Objective function

A completely uniform normal stress distribution cannot be achieved due to the presence of a stress singularity near the edge. Thus, the goal is to minimize the deviation from a uniform stress distribution. The deviation from a uniform stress distribution is quantified as the integral of stress deviation squared over the contact area (referred to as "squared deviation"); for the plane strain case is:

$$\mathrm{Dev}(\sigma_{zz}) = \frac{1}{L}\int_{x=0}^{L} \left(\sigma_{zz} - \sigma_{zz-avg}\right)^2 dx \tag{6}$$

A similar definition of the squared deviation for the axisymmetric case is given in the Appendix Eq. (B2). For the squared deviation defined in Eq. (6) to be meaningful, the integration of Eq. (6) needs to be bounded in the stress singularity dominated region near the edge where the stress distribution is given by Eq. (3). Assuming the length of the stress singularity dominated region is ε, the squared deviation in plane strain condition in the stress singularity dominated region near the edge is:

$$\frac{1}{L}\int_{x=L-\varepsilon}^{L} \left(H(L-x)^{-0.41} - 1\right)^2 dx = \frac{1}{L}\left(\frac{50}{9}H^2\varepsilon^{0.18} - \frac{200}{59}H\varepsilon^{0.59} + \varepsilon\right) \tag{7}$$

which is bounded. Generally, when two elastic materials are adhered together, the stress singularity near the edge takes the form $\sigma_{zz} = H(L\text{-}x)^{\lambda}$, where λ is the order of stress singularity (which is -0.41 for a nearly incompressible material adhered to a rigid material that is studied in this work). λ lies in the range [-0.5, 0], so $-1 \leq 2\lambda \leq 0$. Except for $\lambda = 0.5$, the squared deviation in plane strain condition is always bounded. A smaller squared deviation indicates a more uniform normal stress distribution. The squared deviation is used as the objective function in our analysis, and we minimize the squared deviation to obtain the normal stress distribution that deviates the least from a uniform stress distribution.

From Eqs. (2) and (5) with $\sigma_{zz\text{-}avg} = 1$ we obtain:

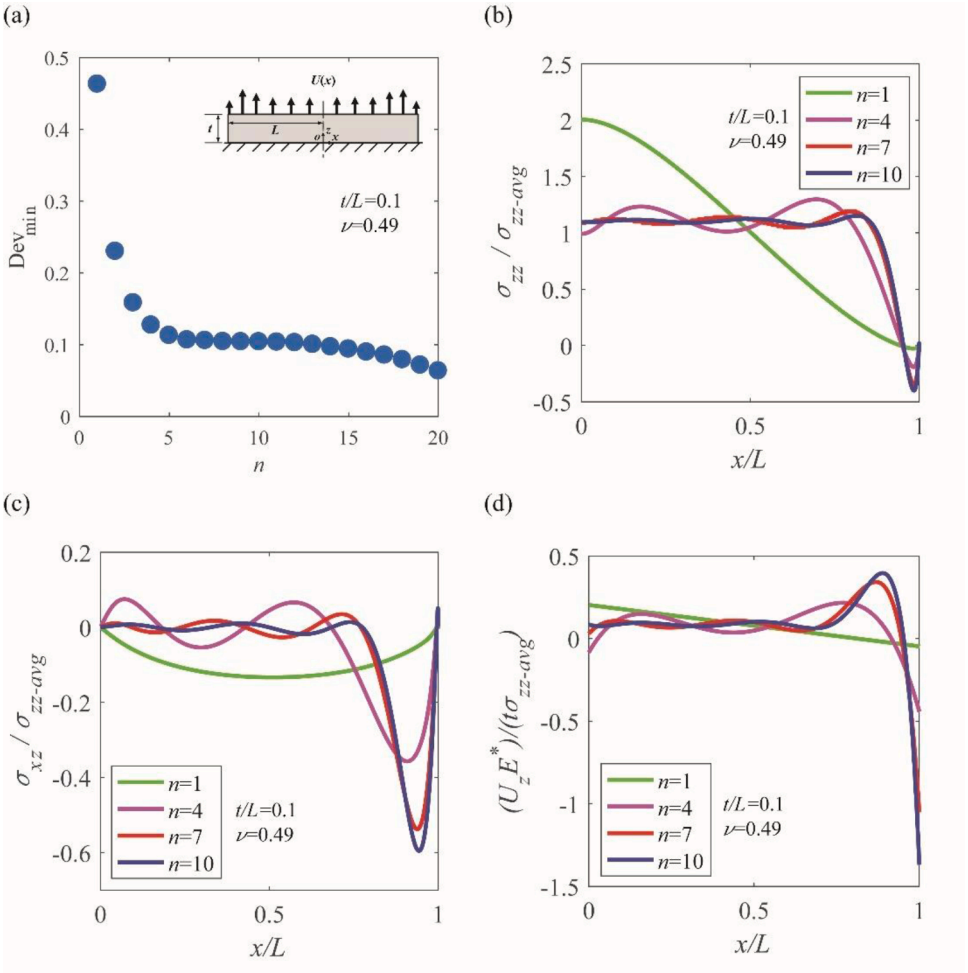

Fig. 2. Optimization results for minimizing the squared deviation under the constraint $H = 0$ for various n with $t/L = 0.1$ (plane strain). (a) Minimum squared deviation achieved as a function of n. (b) Normal stress distribution at the adhered interface for different n. (c) Shear stress distribution at the adhered interface for different n. (d) The required normal displacement to achieve the optimal stress distribution for different n.

$$\mathrm{Dev}(\sigma_{zz}) = \frac{1}{L}\int_{x=0}^{L}\left(\sum_{i=0}^{n} a_i \cdot \left(\sigma_z^i - 1\right)\right)^2 dx \tag{8}$$

which can be rewritten as:

$$\mathrm{Dev}(\sigma_{zz}) = \sum_{i=0}^{n}\sum_{j=0}^{n} A_{ij} \cdot a_i a_j \tag{9}$$

where:

$$A_{ij} = \frac{1}{L}\int_{x=0}^{L}\left(\sigma_z^i - 1\right)\left(\sigma_z^j - 1\right)dx. \tag{10}$$

A_{ij} is calculated from $\sigma_z{}^i$ obtained from FE and these values are constants for a given geometry (i.e. a given t/L). The goal is to minimize the squared deviation.

$$\min_{a_i} \mathrm{Dev}(\sigma_{zz}) \tag{11}$$

and the minimum is obtained when its partial derivative with respect to each independent coefficient (a_i) is 0:

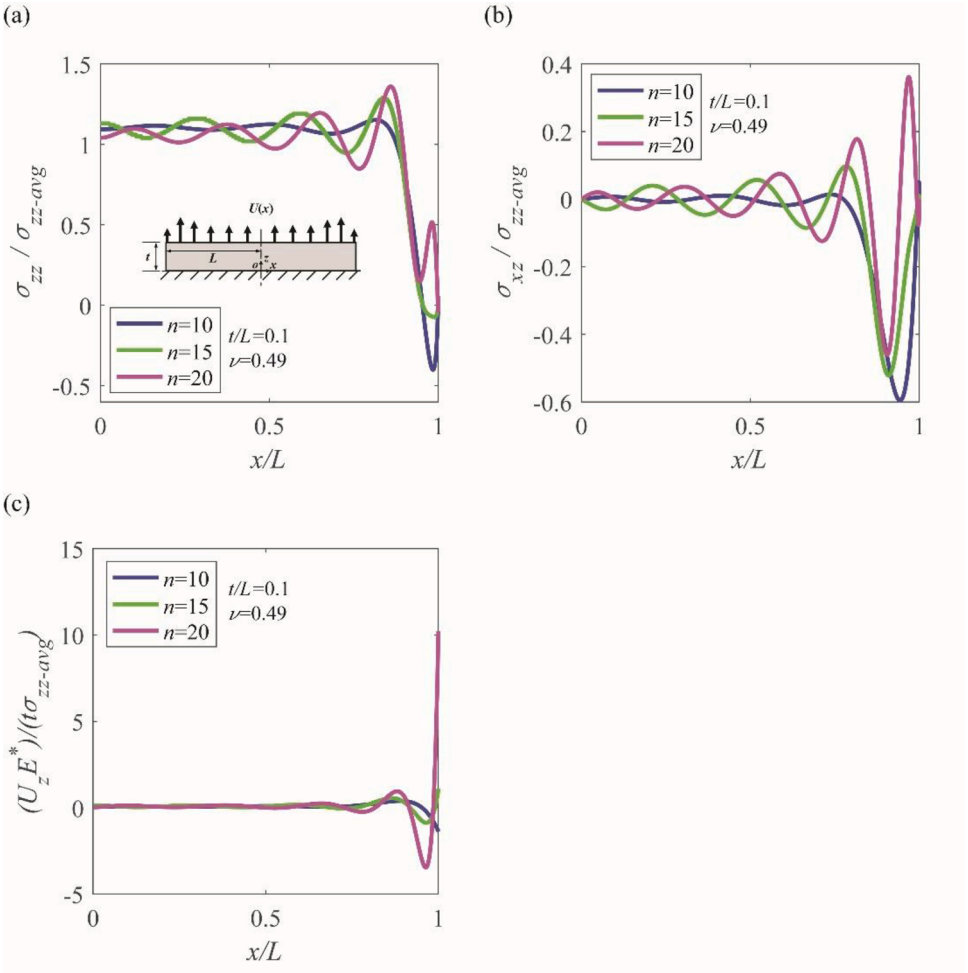

Fig. 3. Optimization results for minimizing the squared deviation under the constraint $H = 0$ for large n with $t/L = 0.1$ (plane strain). (a) Normal stress distribution at the adhered interface for $n = 10$, 15 and 20. (b) Shear stress distribution at the adhered interface for $n = 10$, 15 and 20. (c) The required normal displacement to achieve the optimal stress distribution for $n = 10$, 15 and 20.

$$\frac{\partial \mathrm{Dev}}{\partial a_i} = 0. \tag{12}$$

From Eq. (9), it is clear that $\mathrm{Dev}(\sigma_{zz})$ is a quadratic function of a_i, so Eq. (12) is a set of linear equations about a_i, and the a_i corresponding to the minimum squared deviation for a given order of polynomial series (n) can be determined by solving Eq. (12).

2.3. Constraint

While minimizing the squared deviation leads to a normal stress distribution that has minimum deviation from a uniform stress distribution over the entire contact area, it does not explicitly address the stress concentration locally near the edge. The interface may still fail from the edge due to the presence of a stress concentration (Appendix C). A constraint is added to avoid a reduction in the effective adhesion strength due to stress concentration near the edge. This constraint requires that the normal stress at a point x_0 very close to edge be equal to 0:

$$\sigma_{zz}(x_0 \to L) = \sum_{i=0}^{n} a_i \cdot \sigma_z^i(x_0 \to L) = 0 \tag{13}$$

In implementation, x_0/L is chosen to be 0.99991. Since this point is very close to the edge and is within the stress singularity dominated region (Balijepalli et al., 2017; Luo and Turner, 2020), expressing the normal stress at x_0 in terms of Eq. (3) yields:

$$\sigma_{zz}(x_0) = H(L - x_0)^{-0.41} = 0 \tag{14}$$

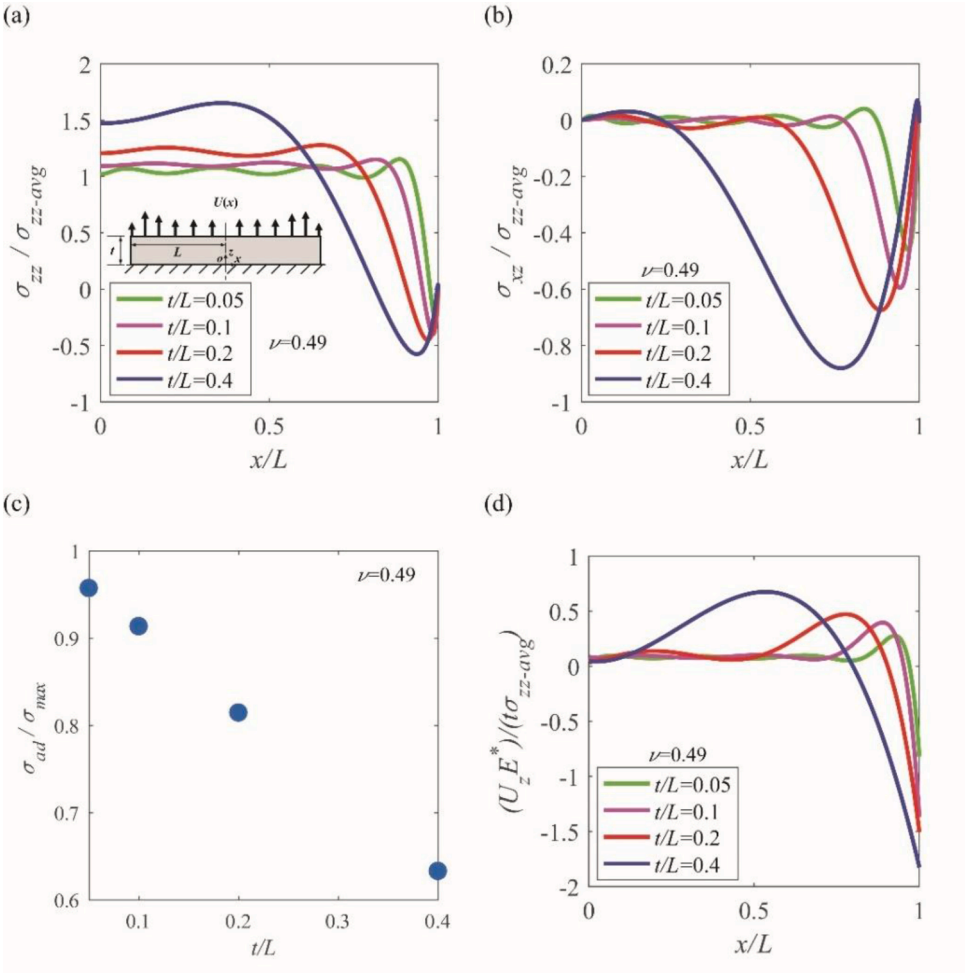

Fig. 4. Practical optimum solutions for layers with different t/L (plane strain). (a) Normal stress distribution at the adhered interface. (b) Shear stress distribution at the adhered interface. (c) Ratio of the adhesion achieved by the practical optimum cases to the maximum adhesion achieved by a completely uniform normal stress distribution. (d) The required normal displacement to achieve the stress distributions.

which indicates that the constraint of Eq. (13) implies that the magnitude of the stress singularity (H) near the edge equals to 0.

With the constraint above, the optimization is conducted first by substituting Eq. (13) into Eq. (9) to obtain a quadratic equation with n independent coefficients, then the partial derivatives of Eq. (9) are taken with respect to remaining n independent coefficients and equating them to 0 (Eq. (12)). By solving the n linear equations for n independent coefficients, the corresponding optimum displacement distribution can be determined. For all the practical optimum normal stress distributions found in this study, there is a small negative H rather than $H = 0$ present near the edge (i.e. compressive stress near the edge). This is because the numerical calculation has finite accuracy and a small residual H is left. A small negative H indicates compressive stress near the edge and this will not adversely impact the adhesion strength.

2.4. Practical limitation on U(x)

The analysis above is based on linear elasticity and does not enforce a limitation on the magnitude of $U(x)$ that would ensure the tip material remains linear elastic. At high strains, a material could exhibit non-linear elastic or plastic behavior and even rupture. As the goal here is to design structures that can be realized in practice, we determine the *practical optimum displacement* distribution by enforcing a limit on the strains within the thin layer.

The applied normal displacement (U_z) is presented in a normalized form $(U_z E^*)/(t\sigma_{zz\text{-}avg})$ in this paper, where $E^* = E/(1\text{-}\nu^2)$. Generally, the theoretical dry adhesion strength, σ_{th}, of a material is estimated to be 1–10% of its modulus (Gao and Chen, 2005; Gao and Yao, 2004; Tang et al., 2005), thus $\sigma_{zz\text{-}avg}/E^*$ should be on the order of 0.1 or less. As a result, the strain (U_x/t) that needs to be applied to the tip layer in a real system is less than or equal to ~0.1 of the normalized normal displacement $(U_z E^*)/(t\sigma_{zz\text{-}avg})$ shown in this paper.

The admissible normalized displacement $(U_z E^*)/(t\sigma_{zz\text{-}avg})$ differs for different materials, and there are two types of materials

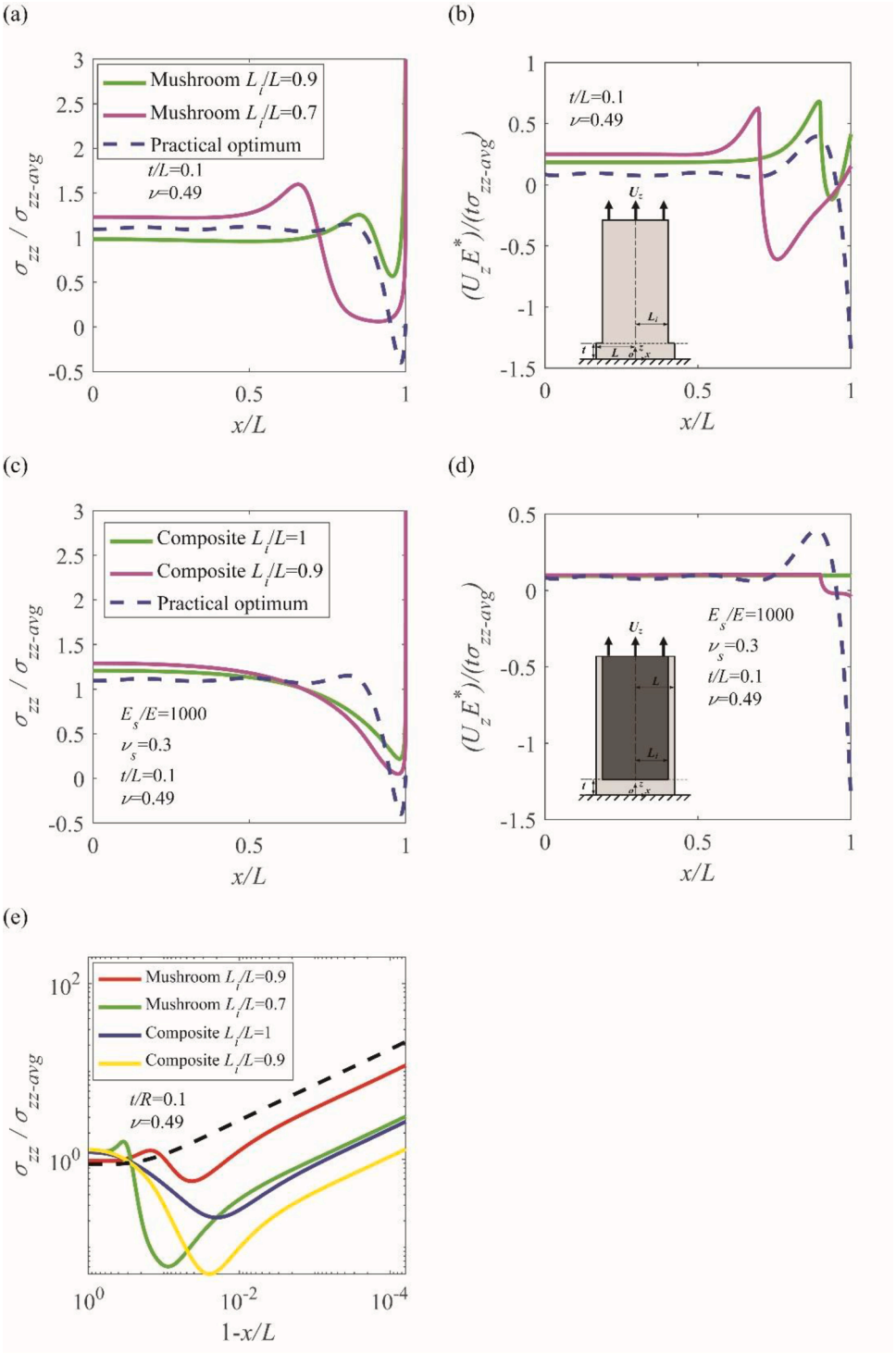

Fig. 5. (a) Normal stress distribution at the adhered interface for mushroom-shaped adhesive structures with $L_i/L = 0.7$ and 0.9 (plane strain) (the maximum value of the y axis is truncated at 3). (b) Normal displacement applied on the top surface of the tip layer for mushroom-shaped structures with $L_i/L = 0.7$ and 0.9 (plane strain). (c) Normal stress distribution at the adhered interface for composite structures with $L_i/L = 0.9$ and 1 (plane strain) (the maximum value of the y axis is truncated at 3). (d) Normal displacement applied on the top surface of the tip layer for composite structures with $L_i/L = 0.9$ and 1 (plane strain). (e) Normal stress distribution at the adhered interface near the edge for mushroom-shaped structures and composite structures (plane strain) (the normal stress distribution near the edge for a homogeneous rectangular structure is shown as a dashed curve for comparison).

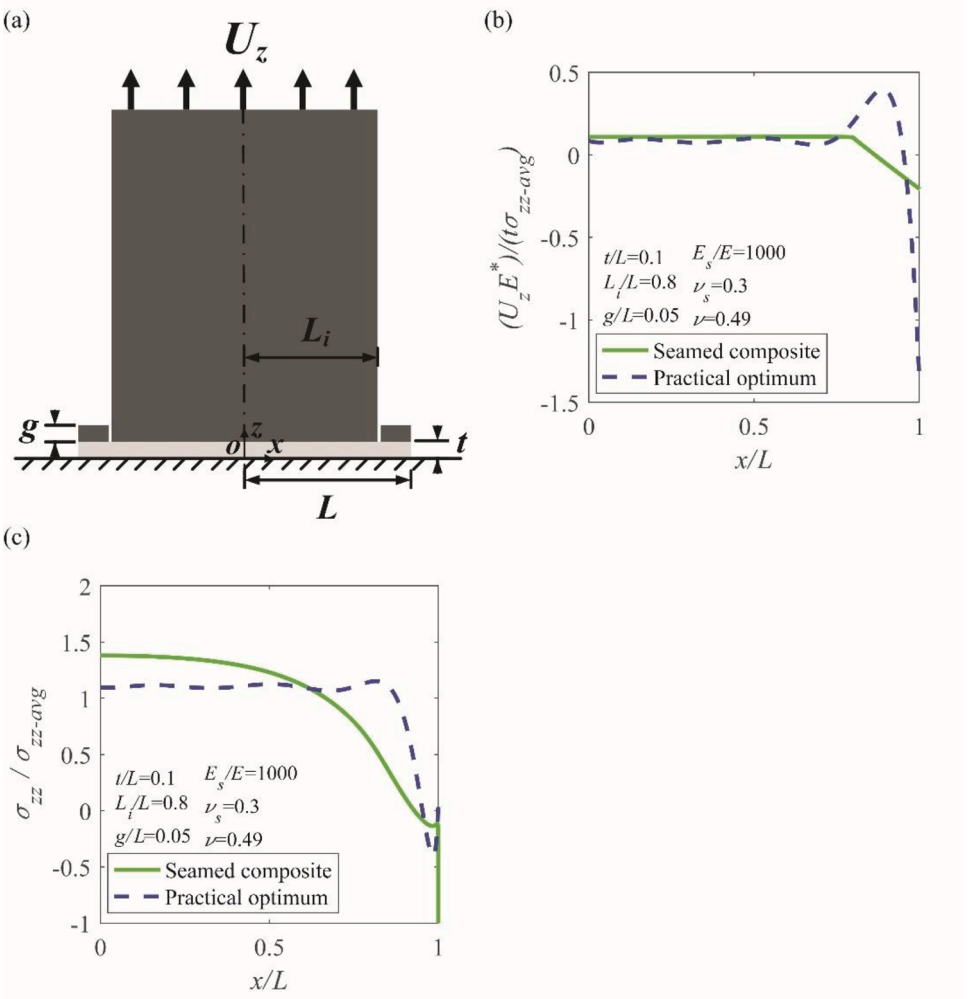

Fig. 6. (a) Schematic of a segmented composite structure (plane strain) (the dark gray region is 1000 times stiffer than the light gray region). (b) Normal displacement applied on the top surface of the tip layer for the segmented composite structure with $t/L = 0.1$, $L_i/L = 0.8$ and $g/L = 0.05$. (c) Normal stress distribution at the adhered interface for the segmented composite structure with $t/L = 0.1$, $L_i/L = 0.8$ and $g/L = 0.05$ (the minimum value of the y axis is truncated at -1).

commonly found in dry adhesives. The first are soft elastomers, where σ_{th}/E^* is ~10% (Tang et al., 2005). Polydimethylsiloxane (PDMS), a commonly used elastomer, exhibits linear elastic behavior up to strains of ~40% and ruptures at strains of ~80% (Johnston et al., 2014; Kim et al., 2011; Schneider et al., 2008; Seghir and Arscott, 2015). Other commonly used elastomers such as Ecoflex (Hsu et al., 2013; Ranzani et al., 2015) generally have larger linear elastic strain limits and rupture strains than PDMS, so PDMS is a conservative choice as a representative material. Using PDMS as a representative material, with $\sigma_{th}/E^* \approx 0.1$ and a linear elastic regime of $-0.4 \leq U_x/t \leq 0.4$, we find that $|(U_z E^*)/(t\sigma_{zz\text{-}avg})|$ must be smaller than 4. The other class of materials in dry adhesives are polymers with moduli of 1–4 GPa, such as polystyrene or keratin. The polymers typically have $\sigma_{th}/E^* = 1$–2% (Gao and Yao, 2004; Tang et al., 2005), and are linear elastic up to strains of 5% (higher strains cause plastic deformation) (Swallowe and Lee, 2006). With $\sigma_{th}/E^* = 0.01$–0.02 and a linear elastic range of $-0.05 \leq U_x/t \leq 0.05$, the normalized displacements $|(U_z E^*)/(t\sigma_{zz\text{-}avg})|$ must be smaller than 2.5–5. All the practical optimum displacements presented in this study exhibit normalized magnitudes smaller than 1.8, which corresponds to a strain $|U_x/t| < 0.18$ for a soft elastomer tip layer and $|U_x/t| < 0.036$ for a stiff material tip layer. As a result, both the material and the geometric deformation are expected to exhibit linear behavior.

3. Finite element modeling

FE analysis was used to find the stress distribution (σ_z^i and τ_z^i, σ_x^i and τ_x^i) at the adhered interface of the tip layer corresponding to each polynomial basis (δ_z^i, δ_x^i) applied on the top surface of the tip layer. Most of the cases studied are in plane strain condition. A flat layer with half width $L = 1$ mm and thicknesses $t = 0.05$, 0.1, 0.2 and 0.4 mm (Fig. 1(c)) is modeled. The material has a Young's modulus $E = 2$ MPa and a Poisson's ratio $\nu = 0.49$. Only half of the layer is simulated with a symmetric boundary condition applied to

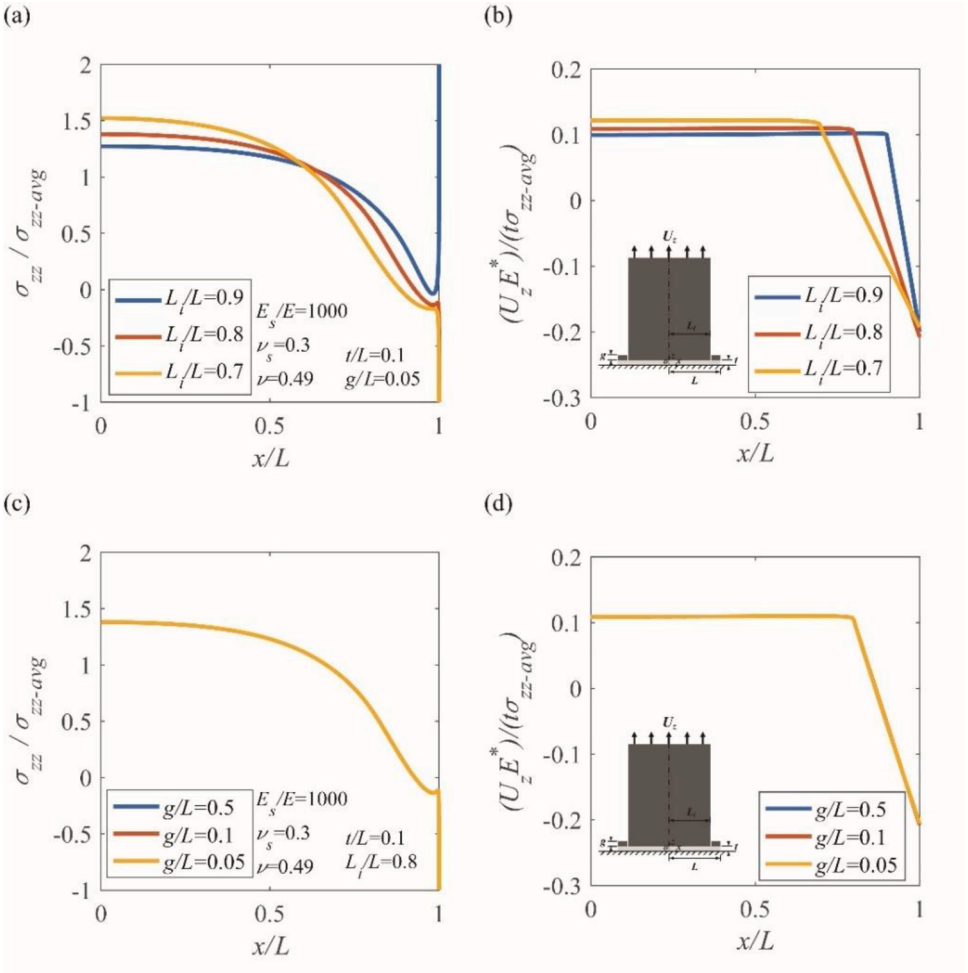

Fig. 7. (a) Normal stress distribution at the adhered interface for segmented composite structures with various L_i/L, $g/L = 0.05$ and $t/L = 0.1$ (plane strain). (b) Normal displacement applied on the top surface of the tip layer for the segmented composite structure with various L_i/L, $g/L = 0.05$ and $t/L = 0.1$ (plane strain). (c) Normal stress distribution at the adhered interface for segmented composite structures with various g/L, $Li/L = 0.8$ and $t/L = 0.1$ (plane strain). (d) Normal displacement applied on the top surface of the tip layer for the segmented composite structure with various g/L, $Li/L = 0.8$ and $t/L = 0.1$ (plane strain).

the centerline. All displacements at the bottom interface are fixed at 0. For the normal displacement polynomial basis of order i ($\delta_z{}^i$), a displacement field with $U_z = 0.001x^i$ mm and $U_x = 0$ is applied on the top surface of the tip layer and $\delta_z{}^i = 0.001x^i/\sigma_{zz\text{-}avg}$. Similarly, for the shear displacement polynomial basis of order i ($\delta_x{}^i$), a displacement field with $U_z = 0$ and $U_x = 0.001x^i$ mm is applied on the top surface of the tip layer and $\delta_x{}^i = 0.001x^i/\ \sigma_{zz\text{-}avg}$.

Commercial FE software, Abaqus Standard (Abaqus 2016, Providence, RI), was used to perform the analysis. Plane strain quadrilateral elements (CPE4RH) were used to mesh the 2D plane strain cases, and axisymmetric quadrilateral elements (CAX4RH) were used to mesh the axisymmetric cases. The mesh near the bottom interface and the free edge was refined, and mesh convergence was performed with further refinement resulting in less than 0.005% difference in the average normal stress. Approximately 6.15×10^5 to 8.83×10^5 elements were used over the range of layer thickness studied here.

4. Results

4.1. Effect of the order of the polynomial series

As generally observed in problems solved with series, the results depend on the order of the polynomial series considered (n in Eq. (1)) and a sufficient order of the series is needed to reach a converged solution. Fig. 2(a) shows the minimum squared deviation obtained as a function of the order of the polynomial series (n) for a layer with $t/L = 0.1$. The minimum squared deviation obtained reduces as n increases and reaches a plateau at $n = \sim 6$, and reduces slightly more when $n > \sim 13$ (Fig. 2(a)). The corresponding normal stress distribution becomes more uniform as n increases and the uniformity is independent of n for $6 \leq n \leq 13$ (Fig. 2(b)). When n is

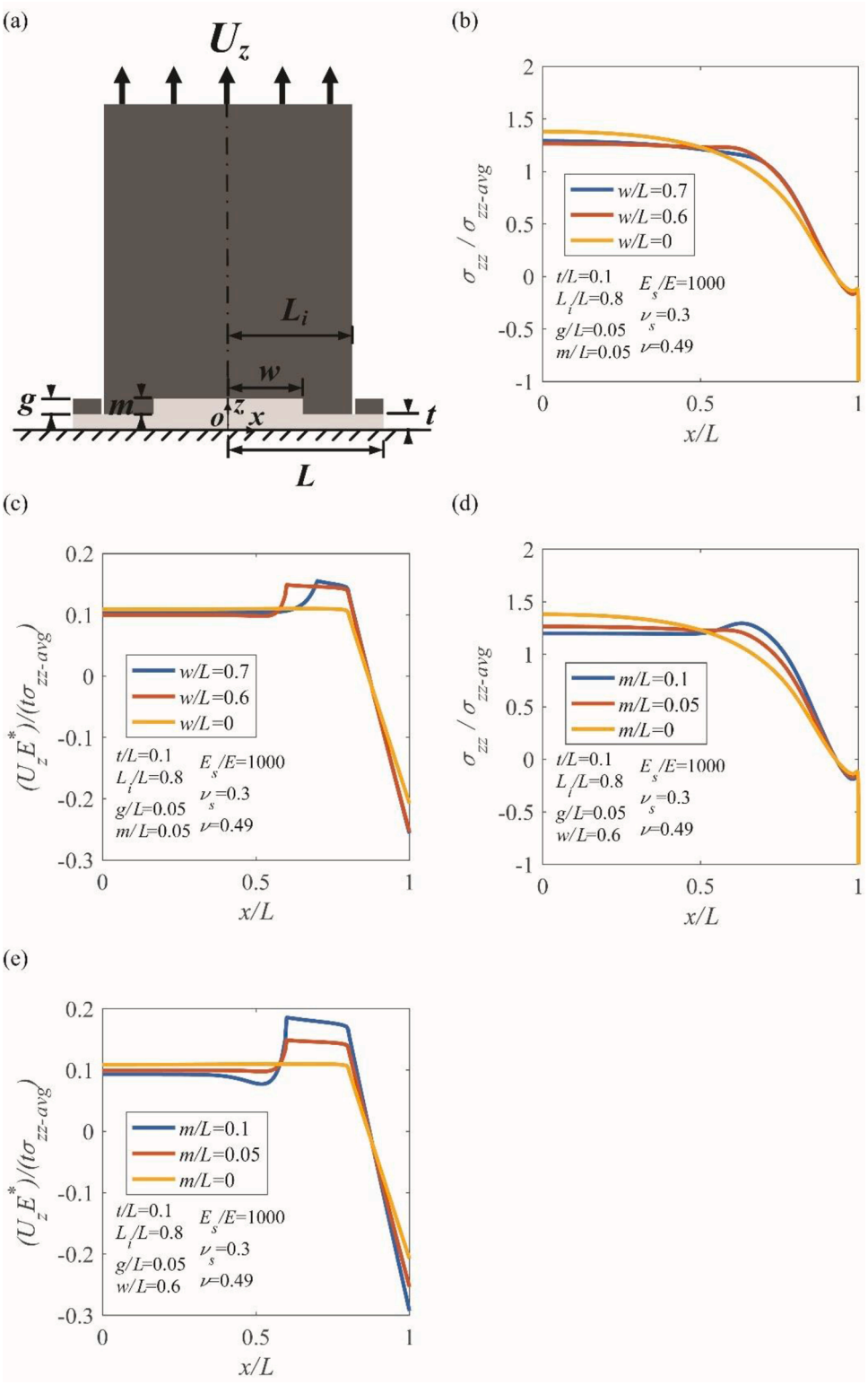

(caption on next page)

Fig. 8. (a) Schematic of a segmented composite structure with a recessed center stalk (plane strain) (the dark gray region is a factor of 1000 stiffer than the light gray region). (b) Normal stress distribution at the adhered interface for the recessed-stalk segmented composite structure with various w/L, $t/L = 0.1$, $L_i/L = 0.8$, $g/L = 0.05$ and $m/L = 0.05$. (c) Normal displacement applied on the top surface of the tip layer for the recessed-stalk segmented composite structure with various w/L, $t/L = 0.1$, $L_i/L = 0.8$, $g/L = 0.05$ and $m/L = 0.05$. (d) Normal stress distribution at the adhered interface for the recessed-stalk segmented composite structure with various m/L, $t/L = 0.1$, $L_i/L = 0.8$, $g/L = 0.05$ and $w/L = 0.6$. (e) Normal displacement applied on the top surface of the tip layer for the recessed-stalk segmented composite structure with various m/L, $t/L = 0.1$, $L_i/L = 0.8$, $g/L = 0.05$ and $w/L = 0.6$.

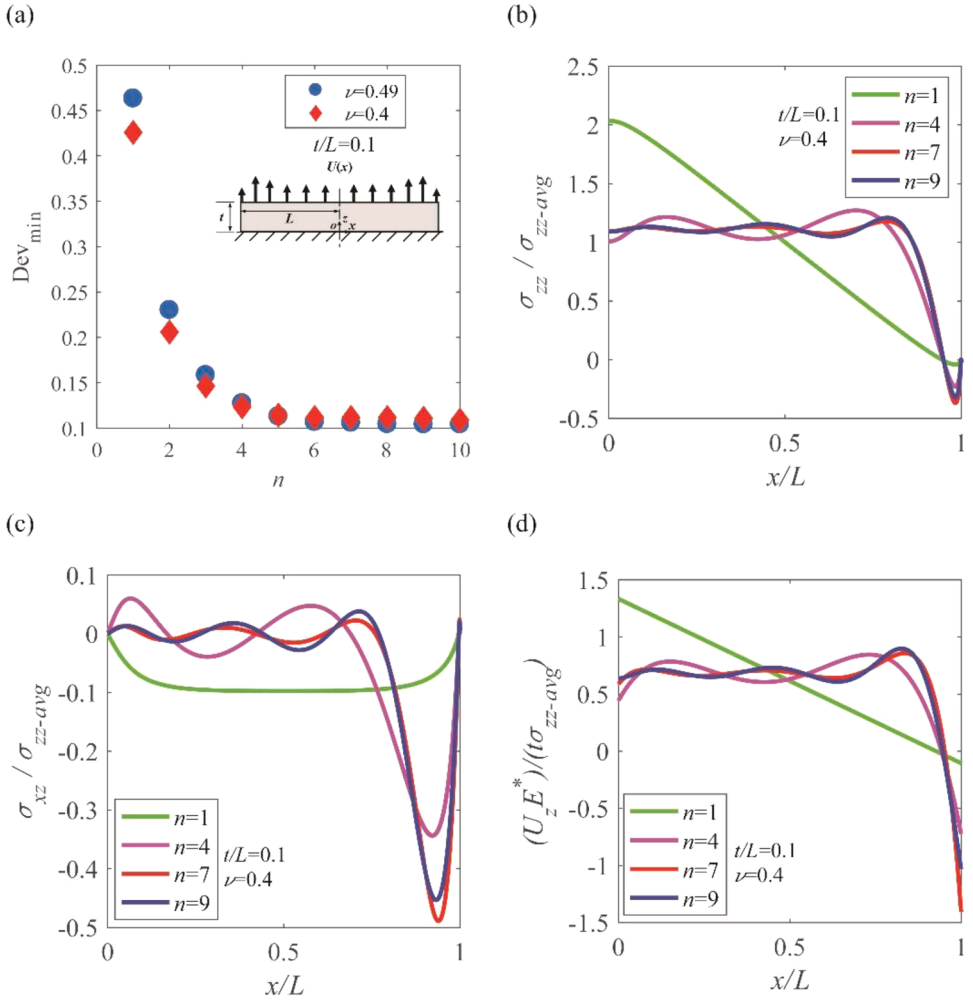

Fig. A1. Optimization results for minimizing the squared deviation under the constraint $H = 0$ for various n with $t/L = 0.1$ and $\nu = 0.4$ (plane strain). (a) Minimum squared deviation achieved as a function of n. (b) Normal stress distribution at the adhered interface for different n. (c) Shear stress distribution at the adhered interface for different n. (d) The required normal displacement to achieve the optimal stress distribution for different n.

increased above 13, there are oscillations in the normal stress distribution (Fig. 3(a)) that are expected to smooth out and converge to another stress distribution for sufficiently high n. The converged normal stress distributions corresponding to $6 \leq n \leq 13$, as seen by the plateau in Fig. 2(a), are considered the *practical optimum normal stress distributions*, since these stress distributions have the minimum deviation from a uniform stress distribution and a displacement that ensures the tip layer is within the elastic limit.

The practical optimum normal stress distribution ($n = 7$ or 10 in Fig. 2(b)) is highly uniform in the center ($\sigma_{zz}/\sigma_{zz\text{-}avg} = 1.09$); the stress starts to decrease at $x/L = \sim 0.85$ to a minimum of $\sigma_{zz}/\sigma_{zz\text{-}avg} = -0.40$ and then increases again to 0 at the edge (due to the presence of a small negative H induced by numerical residual, the normal stress in the numerical calculation increases to a maximum of $\sigma_{zz}/\sigma_{zz\text{-}avg} = 0.019$ at $x/L = 0.9997$ and reduces again for $x/L > 0.9997$). Notably, the normal stress for $x/L > \sim 0.85$ is always smaller than that in the center region and is even in compression in the near edge region. A compressive stress in the near edge region is favorable as it suppresses the crack initiation near the edge, where failure initiates for most interfaces. The corresponding shear stress

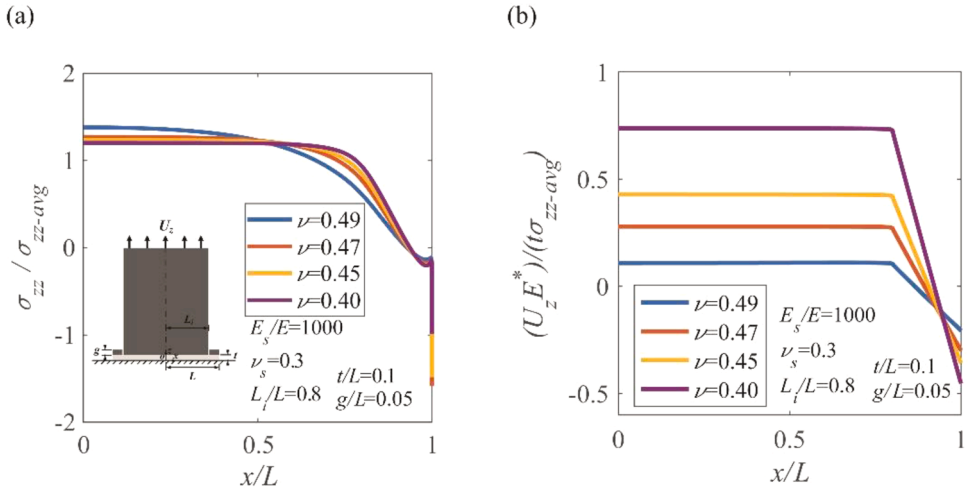

Fig. A2. (a) Normal stress distribution at the adhered interface for segmented composite structures with various tip layer Poisson' ratio ν, L_i/L = 0.8, g/L = 0.05 and t/L = 0.1 (plane strain). (b) Normal displacement applied on the top surface of the tip layer for the segmented composite structure with various tip layer Poisson' ratio ν, L_i/L = 0.8, g/L = 0.05 and t/L = 0.1 (plane strain).

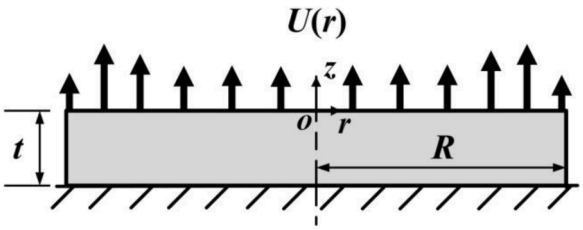

Fig. B1. Schematic of a circular layer adhered to a flat substrate with displacement, $U(r)$, applied on its top surface (axisymmetric).

(n = 7 or 10 in Fig. 2(c)) is nearly 0 in the center and fluctuates near the edge. Since the center region of the contact experiences the highest normal stress and no shear stress, the interface is expected to fail from the center in a mode I failure, and the effective adhesion strength achieved, σ_{ad}, is inversely proportional to the stress level there (Anderson, 2005). Compared to a completely uniform normal stress distribution, the normal stress in center for the practical optimum normal stress distribution is 9% higher, indicating an effective adhesion strength that is 91% of the maximum adhesion strength expected for a uniform normal stress distribution (σ_{ad}/σ_{max} = 0.91). A comparison of the effective adhesion strength between the practical optimum case and several dry adhesive designs is provided below in the Discussion section.

The normal displacement boundary conditions that correspond to these stress distributions are shown in Fig. 2(d). For the practical optimum normal displacement (n = 7 or 10 in Fig. 2(d)), there is uniform tension applied in the center region, an increase in tension between the center and the edge, and compression near the edge. Since the center region of the tip layer is not affected by the presence of the free edge (x/L = 1), a uniform tension applied on the center of the top surface induces a uniform stress distribution in the center of the contact as expected. However, to reach the practical optimum stress distribution near the edge, a specific displacement distribution consisting of the increased tension between the center and the edge and compression near the edge is required. This is evident by comparing the n = 4, 7 and 10 cases. When n reduces from 10 to 4, the region near the edge where the normal stress is lower than that in center has a larger span and the maximum normal stress observed is higher as shown in Fig. 2(b). This is because the region of increased tension and the region of compression near the edge both have smaller maximum magnitudes and are distributed over larger areas for n = 4 (Fig. 2(d)). This observation is helpful in guiding the design of dry adhesives. While the normal stress distribution for n = 4 in Fig. 2(b) has a higher peak stress compared with the practical optimum stress distribution, the peak stress is only 20% higher and the applied displacement becomes less singular (i.e. a less localized displacement boundary condition and a smaller maximum magnitude of displacement). This indicates that a favorable stress distribution can be achieved with a less singular displacement boundary condition, which allows the feature sizes in the structure above the tip layer to be larger and also reduces the strain applied to the tip layer.

For higher n (n > 13 in Fig. 2(a)) there is a different displacement distribution on the top surface of the tip layer (Fig. 3(c)): Instead of compression near the edge, a tensile displacement is observed near the edge, and the magnitude of the tensile displacement increases as n increases. Though it is expected to converge to another normal displacement boundary condition for sufficiently high n which yields a smaller minimum squared deviation than the practical optimum cases, the maximum magnitude of the displacement applied already exceeds the rupture limit of an elastomeric layer and the elastic limit of a stiff layer before it converges (case of n = 20 in Fig. 3

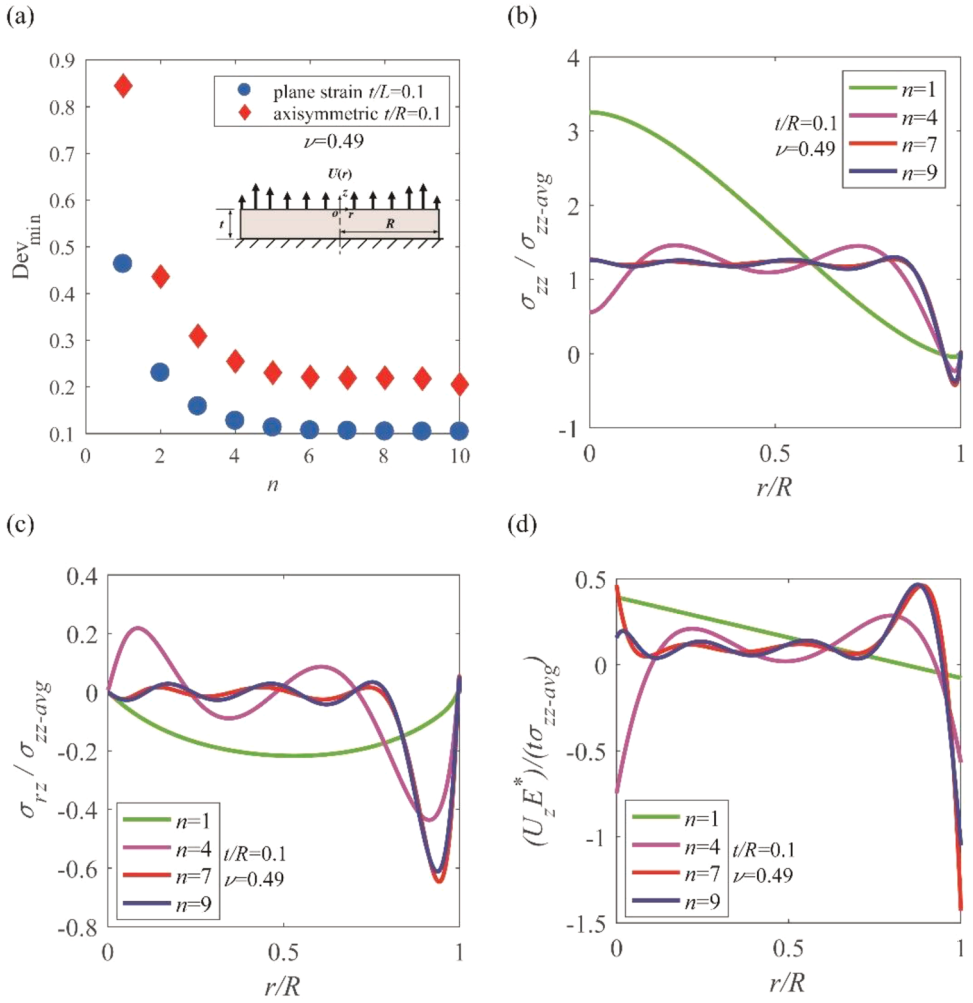

Fig. B2. Optimization results for minimizing the squared deviation under the constraint $H = 0$ for various n for a circular layer with $t/R = 0.1$ (axisymmetric). (a) Minimum squared deviation achieved as a function of n. (b) Normal stress distribution at the adhered interface for different n. (c) Shear stress distribution at the adhered interface for different n. (d) The required normal displacement to achieve the optimal stress distribution for different n.

(c)). Such a solution is impractical for real systems. This also suggests that an analytic solution that contains infinite terms of polynomial series results in an impractical displacement boundary condition too. The practical optimum normal stress distribution ($n = 7$ or 10 in Fig. 2(b)) is thus the optimum normal stress distribution that can be achieved with an admissible displacement boundary condition for a real system. Since most elastomers exhibit Poisson's ratio $\nu = 0.475-0.49$ (Benvidi and Bacca, 2021), we investigate the case of a flat layer of the same thickness $t/L = 0.1$ with Poisson's ratio $\nu = 0.4$ as a bounding case to understand the effect of Poisson's ratio, and the results are summarized in Appendix Fig. A1. When the Poisson's ratio is reduced from 0.49 to 0.4, the practical optimum normal stress distributions are nearly the same, which suggests that the variation of the Poisson's ratio of common elastomers has little effect on the practical optimum stress distribution that can be achieved. However, the magnitude of the corresponding tensile displacement that needs to be applied in the center region to generate the same magnitude of average interfacial stress is ~7 times higher for the case with $\nu = 0.4$ compared to the case with $\nu = 0.49$, which indicates that the center region of a nearly incompressible thin layer exhibits higher tensile stiffness. This is not unexpected since a higher Poisson's ratio leads to more confinement in the center region of a thin layer.

The case of an axisymmetric circular flat layer (Appendix B) with $t/R = 0.1$ is also investigated for comparison. The results are summarized in Appendix Fig. B2. Similar to the plane strain case, the minimum squared deviation reduces as n increases and reaches a plateau at $n = 6$ and reduces again when $n > 9$ as shown in Appendix Fig. B2(a). The converged cases corresponding to n within the plateau region ($6 \leq n \leq 9$) in Appendix Fig. B2(a) are deemed the practical optimum cases and $n > 9$ leads to an impractical applied displacement. The practical optimum normal stress distribution and the corresponding applied displacement ($n = 9$ in Appendix Fig. B2(b) and (d)) are similar to those in a plane strain condition. It should be noted that while the trend and the optimum case shown in Appendix Fig. B2 appear similar to those of the plane strain case, the minimum squared deviation is larger in an

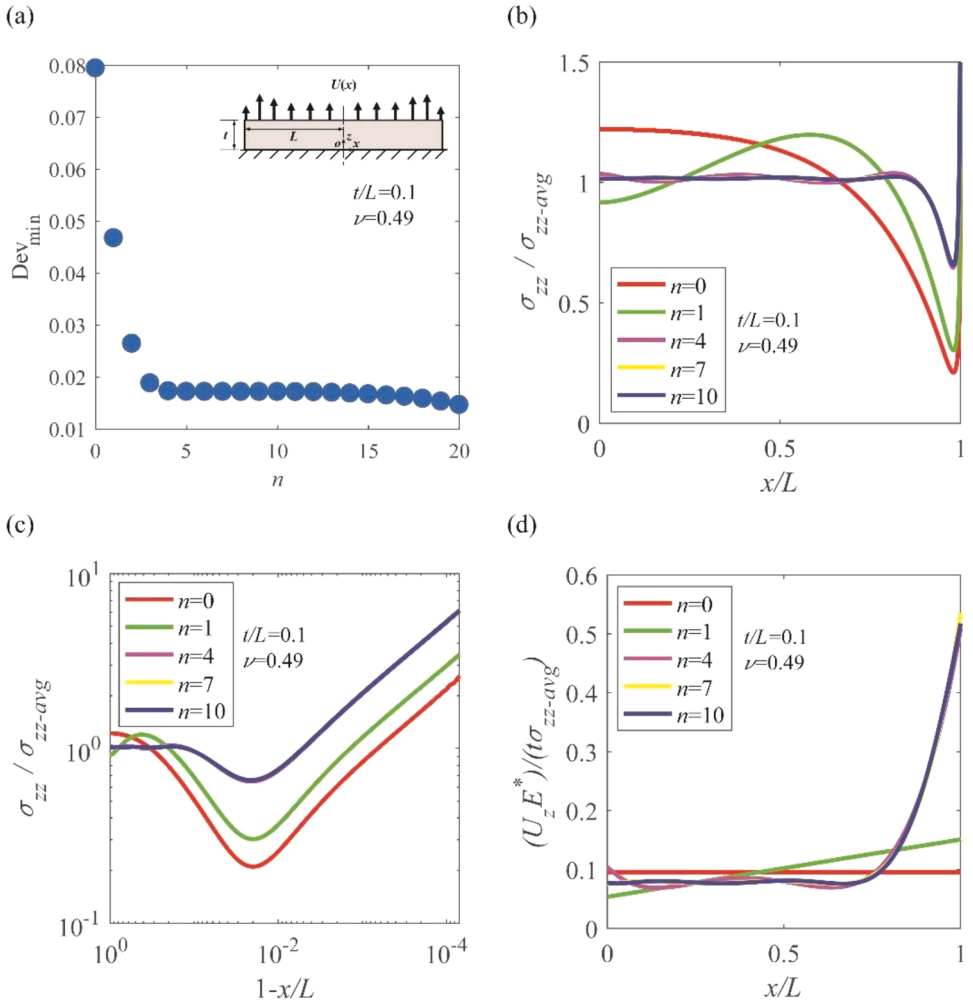

Fig. C1. Optimization results for minimizing the squared deviation for various n with $t/L = 0.1$ (plane strain). (a) Minimum squared deviation achieved as a function of n. (b) Normal stress distribution at the adhered interface for different n (the maximum value of the y-axis is truncated at 1.5). (c) Normal stress distribution at the adhered interface near the edge for different n. (d) The required normal displacement to achieve the optimal stress distribution for different n.

axisymmetric condition for a given n. In the plane strain case, the area is linearly proportional to x, while the area of a layer in axisymmetric condition scales quadratically with r, so the fluctuation in the normal stress near the edge results in a larger squared deviation in the axisymmetric case. This also leads to a higher stress in the center region of the axisymmetric case ($\sigma_{zz}/\sigma_{zz\text{-}avg} = 1.22$) compared to the plane strain case, as the region near the edge with low stress occupies more area and force equilibrium must be maintained.

4.2. *Effect of layer thickness*

The practical optimum stress distributions were determined for various layer thicknesses (t/L) and results are shown in Fig. 4. All the practical optimum cases in Fig. 4 are cases where the solution is insensitive to n (Appendix D). The practical optimum stress distributions (Fig. 4(a)) have similar forms to the results shown in Fig. 2: the normal stress is nearly uniform in the center and decreases near the edge. However, the size of the central uniform region is smaller for higher t/L: $x/L < \sim 0.90$ for $t/L = 0.05$, $x/L < \sim 0.85$ for $t/L = 0.1$, $x/L < \sim 0.71$ for $t/L = 0.2$ and $x/L < \sim 0.47$ for $t/L = 0.4$. As t/L increases, the displacement applied on the top surface of the tip layer is further away from the adhered interface, and its ability to modify the normal stress distribution at the adhered interface decays with increasing distance from the interface, especially in the near edge region. As the center region of the uniform stress distribution becomes smaller for larger t/L, $\sigma_{zz}/\sigma_{zz\text{-}avg}$ in the center region becomes higher due to force equilibrium ($\sigma_{zz}/\sigma_{zz\text{-}avg} = \sim 1.05$ for $t/L = 0.05$, $\sigma_{zz}/\sigma_{zz\text{-}avg} = \sim 1.09$ for $t/L = 0.1$, $\sigma_{zz}/\sigma_{zz\text{-}avg} = \sim 1.22$ for $t/L = 0.2$ and $\sigma_{zz}/\sigma_{zz\text{-}avg} = \sim 1.60$ for $t/L = 0.4$). For the corresponding shear stress distributions (Fig. 4(b)), the shear stress is zero in the center and fluctuates near the edge. Thus, the interface is expected to fail from the center via a mode I failure for all the t/L studied. Fig. 4(c) summarizes the ratio of the effective adhesion achieved by the

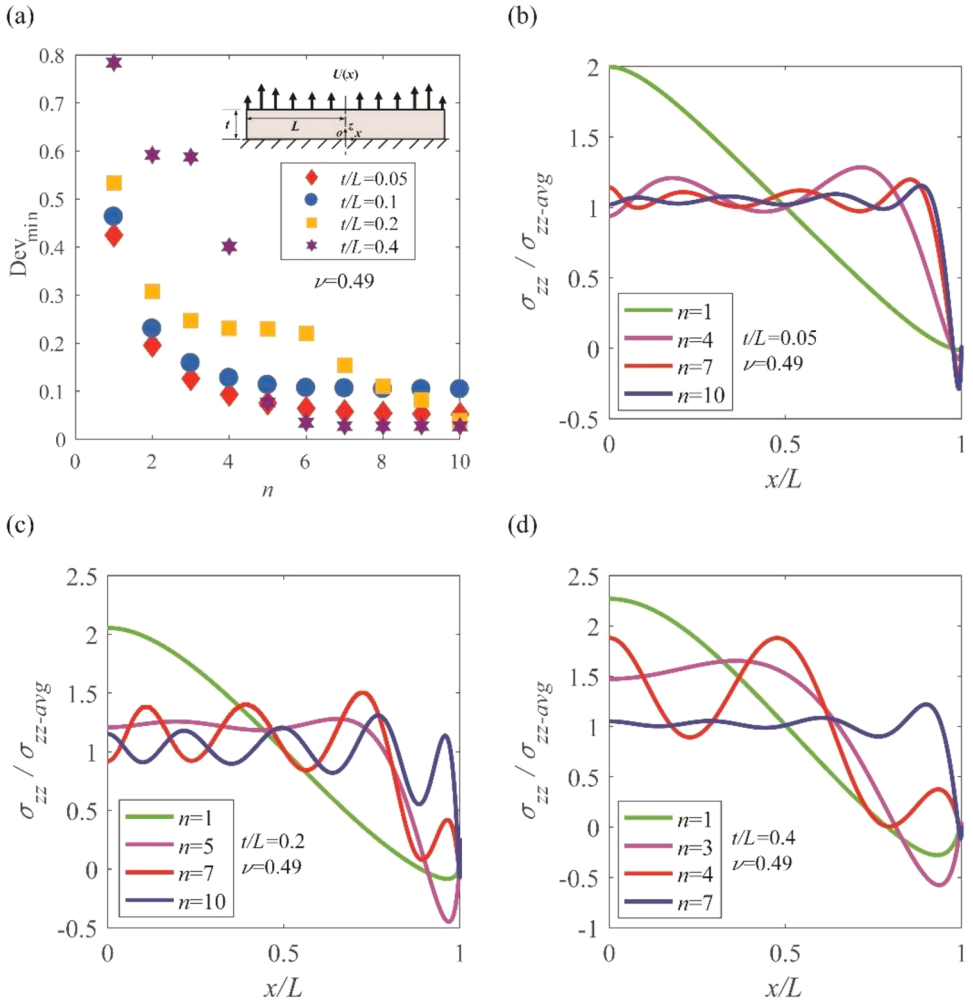

Fig. D1. Optimization results for minimizing the squared deviation under the constraint $H = 0$ for different t/L (plane strain). (a) Minimum squared deviation achieved as a function of n. (b) Normal stress distribution at the adhered interface for $t/L = 0.05$ for different n. (b) Normal stress distribution at the adhered interface for $t/L = 0.2$ for different n. (c) Normal stress distribution at the adhered interface for $t/L = 0.4$ for different n.

practical optimum cases to the maximum adhesion achieved by a completely uniform normal stress distribution for various t/L, and it is clear that the adhesion achieved by practical optimum cases reduces as t/L increases. While these results suggest that a thinner tip layer will result in higher effective adhesion strength, it is important to note that there is a minimum t/L required for the layer to deform to accommodate surface roughness and achieve conformal contact. The applied displacement distributions (Fig. 4(d)) also have similar forms to the results shown in Fig. 2, but the region of increased tension and the region of compression near the edge become larger and the maximum magnitudes of tensile and compressive displacements also increase as t/L increases.

5. Discussion

As noted earlier, common dry adhesive structures can be regarded as a thin layer at the tip of structure that transfers load from the far field to the interface. When the structure is loaded, a specific displacement boundary condition is applied on the top surface of the tip layer which generates a specific stress distribution at the adhered interface. In this section, we discuss the design of dry adhesive from this perspective with guidance from the optimization results presented above. The normal displacement boundary condition on the top surface of the tip layer and the normal stress distribution at the adhered interface are investigated and compared with the practical optimum cases. All cases discussed in this section assume plane strain (axisymmetric cases are included in the appendices).

5.1. *Mushroom-shaped and composite adhesive structures*

As the most investigated dry adhesive structures, mushroom-shaped structures and composite structures (Fig. 1(a) and (b)) are considered first. The mushroom-shaped structure is treated as a flat tip layer with $t/L = 0.1$, and a stalk with half width $L_i/L = 0.7$ or 0.9

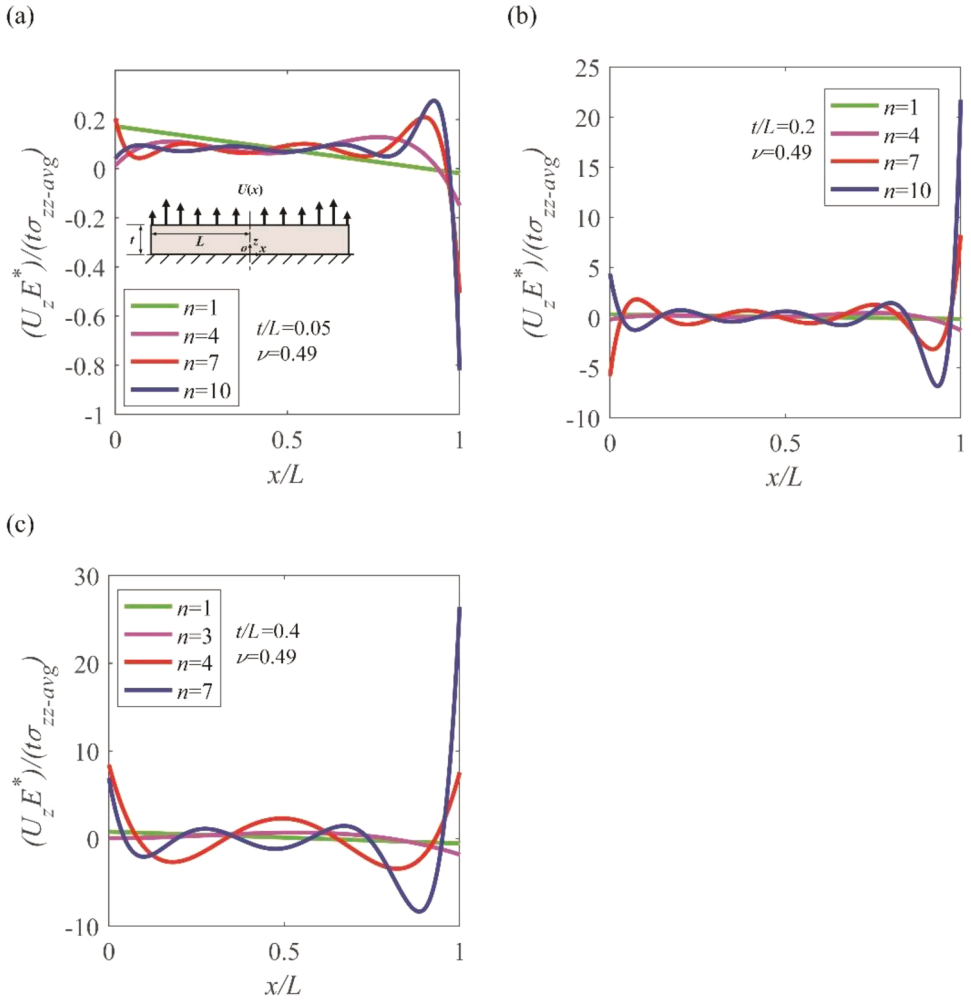

Fig. D2. The required normal displacement to achieve the optimal stress distribution for different t/L (plane strain). (a) Normal displacement applied on the top surface for $t/L = 0.05$ for different n. (b) Normal displacement applied on the top surface for $t/L = 0.2$ for different n. (c) Normal displacement applied on the top surface for $t/L = 0.4$ for different n.

connected to the tip layer. The composite structure has a tip layer with $t/L = 0.1$, and a stiff core with half width $L_i/L = 0.9$ or 1 connected to the tip layer. The stiff core has a Young's modulus $E_s/E = 1000$, and Poisson's ratio $\nu_s = 0.3$ (Minsky and Turner, 2017), where E is the modulus of the tip layer and shell.

The normal stress distributions for mushroom-shaped structures are shown in Fig. 5(a). Although the normal stress distribution is uniform in the center, two stress concentrations are observed: one underneath the edge of the stalk and another near the edge of the tip layer. The peaks in normal stress seen can be understood by the normal displacement applied on the top surface of the tip layer as shown in Fig. 5(b). Similar to the practical optimum case, the normal displacement applied on the top surface of the tip layer for mushroom-shaped structures is a uniform tension in the center, followed by an increase in tension to a local peak and a subsequent decrease in tension as x/L increases. The magnitude and position of this local peak in normal displacement is not as optimized as in the practical optimum case, which leads to the stress concentration underneath the edge of the stalk. A more important difference is the normal displacement applied near the edge. As opposed to the practical optimum case where the normal displacement continually decreases near the edge, the normal displacement on the top surface of the tip layer for a mushroom-shaped structure starts to increase near the edge. This increase in normal displacement leads to the high stress concentration near the edge and may limit the adhesion strength.

For composite structures, the normal stress in the center region is higher than that of the practical optimum case, and the stress concentration near the edge still exists (Fig. 5(c)). For $L_i/L = 0.9$, the normal displacement is uniform in the center and becomes slightly compressive near the edge due to the compliance of the shell (Fig. 5(d)). For $L_i/L = 1$, the normal displacement applied on the top surface of the tip layer is a uniform tension over the entire area. This case of $L_i/L = 1$ suggests that even for a thin tip layer ($t/L = 0.1$) that applying a uniform displacement on the top surface of the tip layer is not sufficient to eliminate the stress concentration near the edge and obtain an optimized stress distribution. Moreover, as the tip layer thickness increases (but is still not sufficiently thick for the

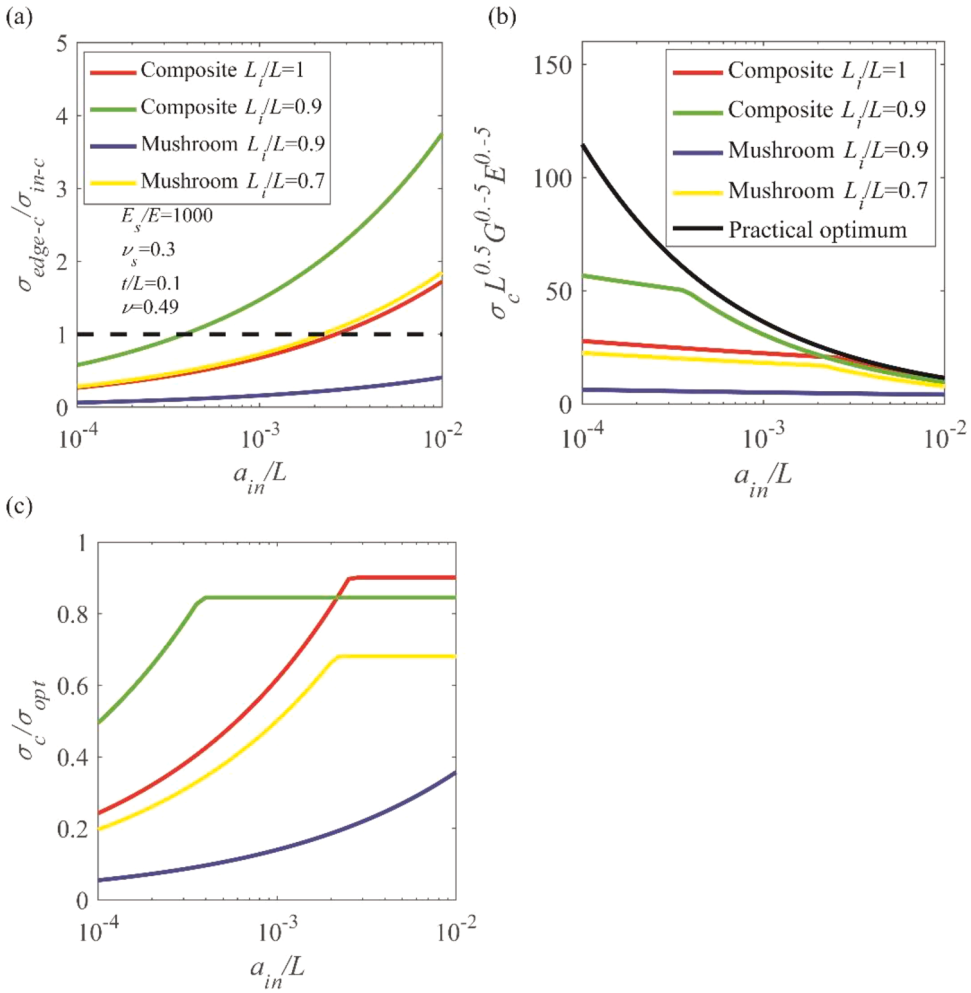

Fig. E1. (a) ratio of the edge crack failure strength to the internal crack failure strength as a function of the internal crack size for mushroom-shaped structures and composite structures. (b) nondimensionalized adhesion strength of mushroom-shaped structures, composite structures and practical optimum case as a function of the internal crack size. (c) ratio of the adhesion strength of mushroom-shaped structures and composite structures to the adhesion strength of the practical optimum case as a function of the internal crack size.

displacement distribution applied on the top surface to not affect the stress distribution at the adhered interface), the optimized normal displacement deviates more from a uniform displacement as shown Fig. 4 and the deficiency of applying a uniform displacement is expected to become more significant.

To highlight the details of the stress singularity near the edge, the normal stress distributions for mushroom-shaped structures and composite structures (Fig. 5(a) and (c)) are replotted on a logarithmic scale in Fig. 5(e). The linear regions in this logarithmic plot indicate the edge singularity dominated region, and the intercept of these lines are log$H$ in Eq. (3). Though neither mushroom-shaped structures nor composite structures eliminate the stress concentration near the edge completely, they exhibit lower normal stress within the stress singularity dominated region compared to a simple homogeneous pillar, and the composite structure with $L_i/L = 0.9$ has the lowest among them. The effective adhesion strength of the practical optimum case and mushroom-shaped structures and composite structures are compared using a linear elastic fracture mechanics-based analysis (Appendix E) and the results are summarized in Appendix Fig. E1. The practical optimum case is found to have higher adhesion strength compared to those mushroom-shaped structures and composite structures, but the adhesion enhancement of the practical optimum case relative to those structures depends on the ratio of defect (i.e. crack) size to width of the tip layer (Appendix Fig. E1(c)). As the defect size is reduced, both the mushroom-shaped structures and composite structures will fail from delamination that initiates at the edge due to the stress concentration and the adhesion strength of the practical optimum case is higher. A smaller defect size always leads to higher adhesion strength (Appendix Fig. E1(b)) and the defect size is expected to decrease with better conformability at the contact. Moreover, it was experimentally observed that a cylindrical composite structure with core radius $R_i/R = 0.9$ and compliant tip layer thickness $t/R = 0.13$ still failed from the edge (Minsky and Turner, 2017). This suggests that although the stress concentration near the edge is reduced for mushroom-shaped structures and composite structures, it can still be the dominant stress concentration that causes failure and

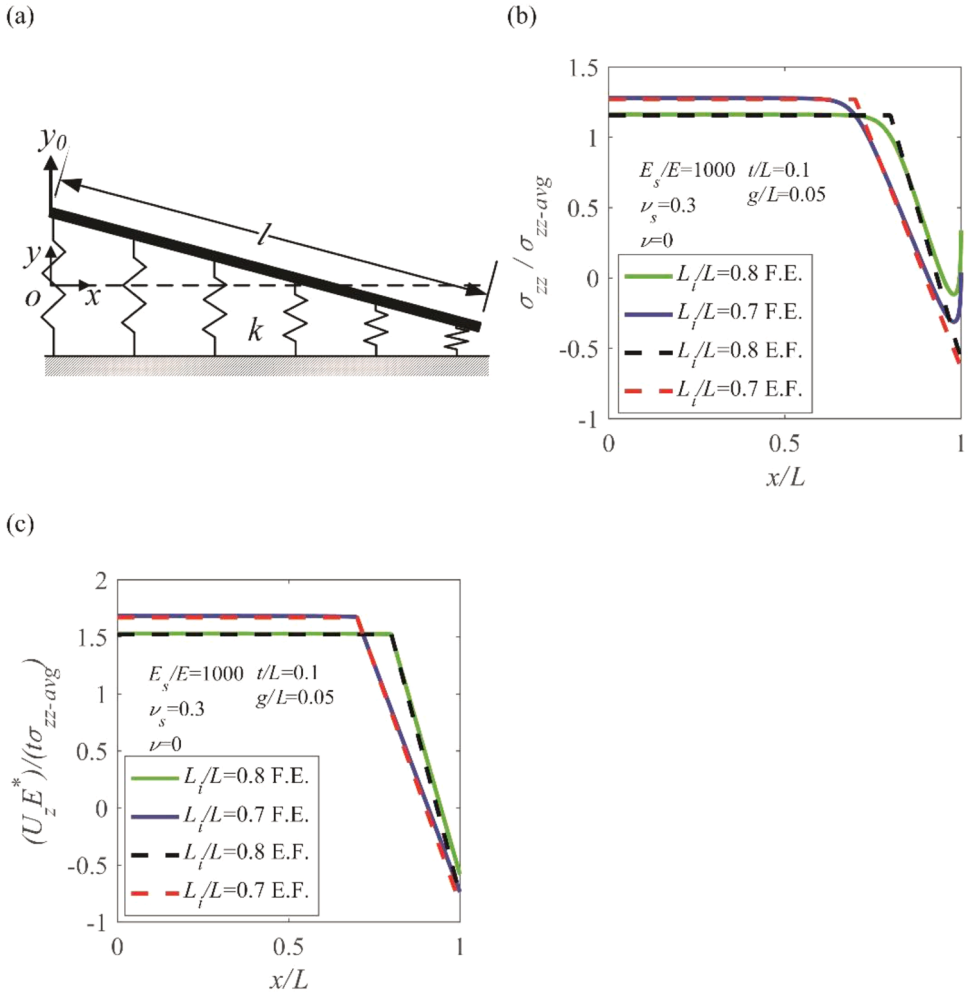

Fig. F1. (a) Schematic of a rigid plate bonded to an elastic foundation being displaced at one end. (b) Comparison of the normal stress distribution at the adhered interface predicted by FE (denoted as F.E.) and the elastic foundation model (denoted as E.F.). (c) Comparison of the normal displacement applied on the top surface of the tip layer predicted by FE (denoted as F.E.) and the elastic foundation model (denoted as E.F.).

leads to a significant reduction in adhesion compared to the practical optimum case.

5.2. *Segmented composite adhesive structure*

The design of a specific structure above the tip layer that provides the practical optimum displacement boundary condition (e.g. Fig. 2) independent of the elastic modulus and theoretical adhesion strength of the material is complex and beyond the scope of the current study. However, a relatively simple structure that generates a displacement boundary condition that achieves the key characteristics of the practical optimum case is presented. As noted above, a critical limitation of mushroom-shaped structures and composite structures is that compressive displacements applied near the edge of the top surface of the tip layer are either absent or not sufficient to fully suppress the stress concentration near the edge of the contact. To generate compression near the edge from remote tension, we propose and analyze a segmented composite structure (Fig. 6(a)) that is inspired by the practical optimum displacement distribution (Fig. 2). The segmented composite structure can be potentially fabricated through a multimaterial 3D printing process (Smith et al., 2020). The structure above the compliant tip layer ($t/L = 0.1$) is comprised of a long stiff center stalk with half width $L_i/L = 0.8$ and a stiff edge plate with thickness $g/L = 0.05$ that covers the rest of the tip layer. Notably, the stiff center stalk and stiff edge plate are not connected. The center stalk and the edge plate have Young's modulus $E_s/E = 1000$, and Poisson's ratio $\nu_s = 0.3$, where E is the modulus of the tip layer.

The normal displacement on the top surface of the tip layer for the segmented composite structure is shown in Fig. 6(b). The normal displacement underneath the stiff center stalk is a uniform tension, like the composite structure (Fig. 5(d)). Outside of the stalk region, the displacement decreases linearly with increasing x/L and is compressive near the edge. The linear decrease in the normal displacement is a result of the stiff edge plate rotating downwards at the edge when the center of the tip layer is loaded in tension,

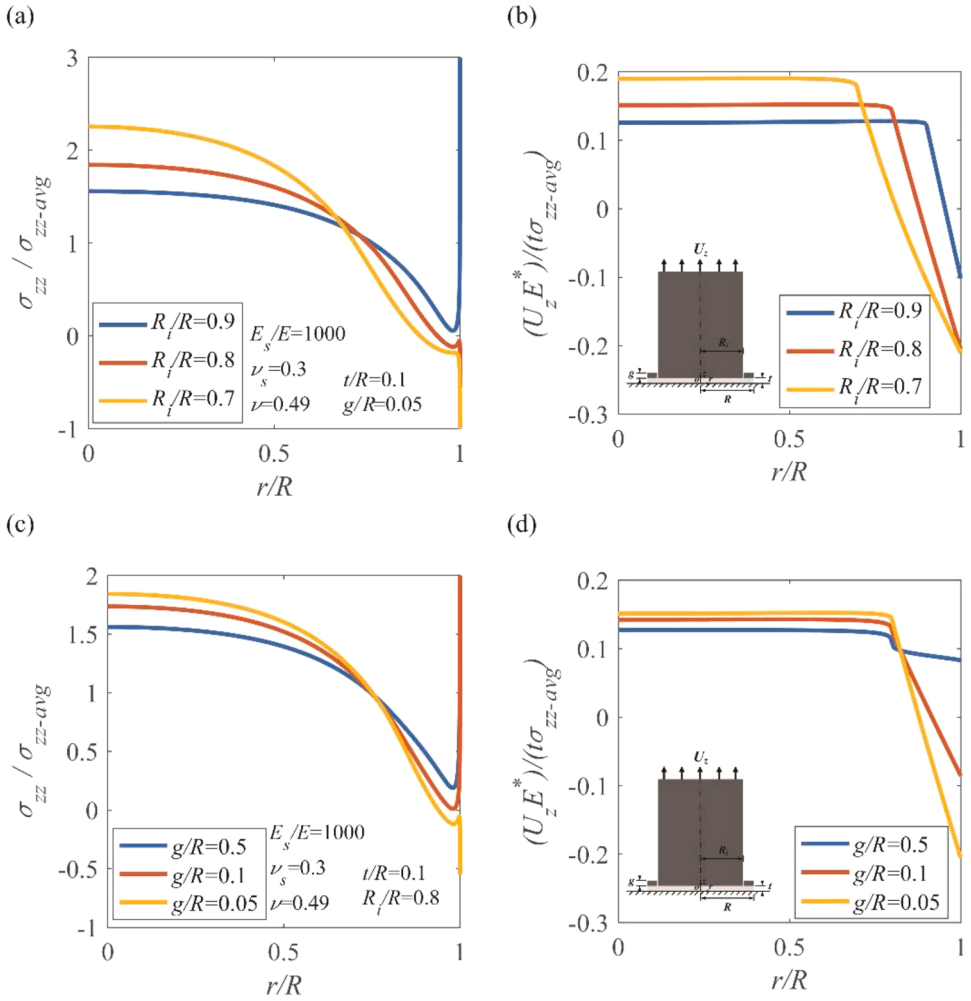

Fig. G1. (a) Normal stress distribution at the adhered interface for segmented composite structures with various L_i/L, $g/L = 0.05$ and $t/L = 0.1$ (axisymmetric). (b) Normal displacement applied on the top surface of the tip layer for the segmented composite structure with various L_i/L, $g/L = 0.05$ and $t/L = 0.1$ (axisymmetric). (c) Normal stress distribution at the adhered interface for segmented composite structures with various g/L, $L_i/L = 0.8$ and $t/L = 0.1$ (axisymmetric). (d) Normal displacement applied on the top surface of the tip layer for the segmented composite structure with various g/L, $L_i/L = 0.8$ and $t/L = 0.1$ (axisymmetric).

which could be understood qualitatively by considering a rigid plate bonded to an elastic foundation being displaced at one end as shown in Appendix F. The corresponding normal stress distribution (Fig. 6(c)) is similar to that of the composite structures (Fig. 5(c)), except that the normal stress near the edge is in compression rather than in tension due to the compressive displacement applied on the top surface of the tip layer. This compressive stress suppresses failure at the edge and the structure is expected to delaminate from the center where the normal stress is highest. Based on the stresses at the center, the segmented composite structure is expected to achieve 72% of the strength that would be achieved by a uniform normal stress distribution. This is 79% of the adhesion achieved by the practical optimum case described above. This design is expected to offer the greatest advantage over mushroom-shaped structures and composite structures when defects at the interface are small compared to the width of the tip layer. As Poisson's ratio of elastomers can vary from 0.475 to 0.49 (Benvidi and Bacca, 2021), the effect of the tip layer's Poisson's ratio on the interfacial stress distribution of the segmented composite structure is also investigated and is shown in Fig. A2(a). When the Poisson's ratio is reduced from 0.49 to 0.4, the normal stress near the edge is still in compression, while the peak stress in the center reduces slightly from 1.38 to 1.20 due to reduced confinement of a lower Poisson's ratio tip layer. The reduction of the peak stress in the center for a composite structure with decreasing Poisson's ratio has also been observed in Benvidi and Bacca (2021). The results here suggest that the segmented composite structure is still able to suppress failure at the edge and achieve high adhesion strength when the Poisson's ratio of tip layer varies from 0.49 to 0.4. The corresponding normal displacement on the top surface of the tip layer for the segmented composite structure is shown in Fig. A2 (b).

The effect of the key dimensions of the segmented composite structure is studied and summarized in Fig. 7. As the half width of the center stalk (L_i/L) reduces, the region of tensile displacement on the top surface of the tip layer becomes smaller, and the compressive

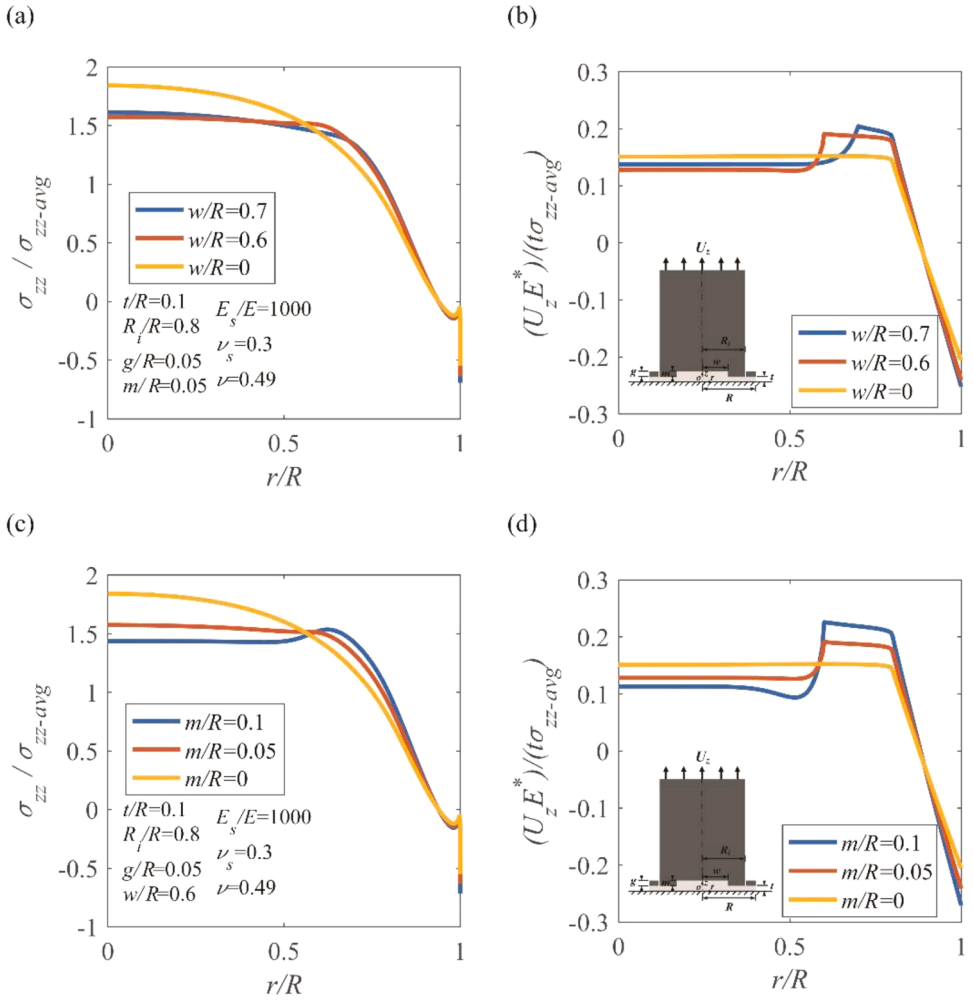

Fig. G2. (a) Normal stress distribution at the adhered interface for the recessed-stalk segmented composite structure with various w/L, $t/L = 0.1$, $L_i/L = 0.8$, $g/L = 0.05$ and $m/L = 0.05$ (axisymmetric). (b) Normal displacement applied on the top surface of the tip layer for the recessed-stalk segmented composite structure with various w/L, $t/L = 0.1$, $L_i/L = 0.8$, $g/L = 0.05$ and $m/L = 0.05$ (axisymmetric). (c) Normal stress distribution at the adhered interface for the recessed-stalk segmented composite structure with various m/L, $t/L = 0.1$, $L_i/L = 0.8$, $g/L = 0.05$ and $w/L = 0.6$ (axisymmetric). (d) Normal displacement applied on the top surface of the tip layer for the recessed-stalk segmented composite structure with various m/L, $t/L = 0.1$, $L_i/L = 0.8$, $g/L = 0.05$ and $w/L = 0.6$ (axisymmetric).

displacement near the edge dominates over larger area (Fig. 7(b)). As a result, the normal stress near the edge changes from tension ($L_i/L = 0.9$) to compression ($L_i/L = 0.8$ and 0.7) and the magnitude of compressive stress increases as L_i/L decreases (Fig. 7(a)). The thickness of the edge plate (g/L) is found to have no effect on the normal stress distribution at the interface and the normal displacement applied on the top surface of the tip layer (Fig. 7(c) and (d)). As long as the edge plate is sufficiently stiff compared to the tip layer, it rotates rigidly downwards when the center of the tip layer is loaded and this is not affected significantly by its thickness over the range examined. The case of an axisymmetric circular composite segmented structure is also studied and the results are summarized in Appendix Fig. G1. The effect of the center stalk radius in axisymmetric condition is similar to the effect of center stalk width in the plane strain case. However, the edge plate thickness in axisymmetric condition is found to significantly affect the interfacial normal stress distribution and the normal displacement applied on the top surface of the tip layer. The magnitude of the compressive displacement near the edge becomes smaller and the corresponding normal stress near the edge becomes tensile as the plate thickness increases. This is because the edge plate is a ring in this case, and a hoop constraint that inhibits the edge plate from rotating downward becomes more significant as the edge plate thickness increases.

As discussed above, the compressive stress near the edge is primarily generated by the edge plate rotating downward and is not significantly affected by the center stalk design. This allows us to further optimize design of the center stalk while maintaining compressive stress near the edge with the edge plate. This idea is demonstrated by a segmented composite structure with a recessed center stalk (Fig. 8(a)). Fig. 8 shows that tuning the design of the center stalk leads to a more uniform normal stress distribution and a normal displacement on the top surface of the tip layer that is closer to the optimum normal displacement compared to the design

shown in Fig. 6(a). Such a design was also considered for the axisymmetric case and the results are similar to those in plane strain condition as shown in Appendix Fig. G2.

Note that the analysis in this paper assumes that the bottom interface of the adhesive layer is perfectly bonded to the substrate; this assumption is widely adopted in analyzing dry adhesive structures (Balijepalli et al., 2017, 2016; Fleck et al., 2017; Khaderi et al., 2015; Luo et al., 2020). Furthermore, the analysis assumes that detachment will initiate at a region of high stress from which an interface crack will propagate. Because of the finite strength and finite range of the adhesive forces at the interface, there will a cohesive zone at the tip of this crack. The assumptions and analysis in this paper are appropriate as long as the size of the cohesive zone is small relative to the size of adhesive structure. Previous work has shown that for adhesive structures below a critical size that the behavior of the cohesive zone can dominate and the structure can become shape or flaw insensitive (Gao and Yao, 2004; Jiang et al., 2014; Tang et al., 2005). While such cases would not be covered by the present analysis, most dry adhesive structures do not fall in this regime (Gao and Yao, 2004; Jiang et al., 2014).

6. Conclusion

The effective adhesion strength of dry adhesive structures can be enhanced by improving the stress uniformity at the adhered interface and suppressing the singular stress concentration at the edge. An optimization approach was developed and used to determine the displacement that must be applied on the top surface of a thin elastic layer to minimize the deviation from a uniform interface stress distribution and to suppress the edge stress concentration. The practical optimum displacement was determined to be a distribution in which there is uniform tensile displacement in the center, a peak displacement between the center and the edge, and a compressive displacement near the edge. The effective adhesion strength achieved with this practical optimum case increases as the layer thickness (t/L) decreases, but the tip layer must be sufficiently thick to allow for conformal contact.

Several dry adhesive designs were compared to the practical optimum case that was determined. Both mushroom-shaped and composite structures provide insufficient compression near the edge to remove the stress concentration. To eliminate the potential for edge failure, a segmented composite structure was proposed and analyzed. The support structure for the compliant tip layer for the segmented composite structure consists of a stiff center stalk and a stiff edge plate. The segmented composite structure results in a normal stress distribution at the adhered interface that is similar to that of composite structures with the key difference that the normal stress near the edge is in compression rather than in tension. The segmented composite structure is predicted to have an adhesion strength that is 79% of what would be achieved by the practical optimum case.

CRediT authorship contribution statement

Aoyi Luo: Conceptualization, Formal analysis, Investigation, Validation, Writing – original draft, Writing – review & editing. **Kevin T. Turner:** Conceptualization, Supervision, Writing – review & editing, Data curation.

Declaration of Competing Interest

The authors declare that they have no known competing financial interests or personal relationships that could have appeared to influence the work reported in this paper.

Acknowledgment

This work was supported by the National Science Foundation under awards 1663037 and 1761726. The authors thank Professor John L. Bassani, Professor Prashant K. Purohit, Christopher Stabile and Sumukh Shankar Pande for providing helpful comments on the manuscript.

Appendix A. Effect of the Poisson's ratio

A thin layer of thickness $t/L = 0.1$ with Poisson's ratio $\nu = 0.4$ in plane strain is examined and the results are summarized in Fig. A1.

The effect of the Poisson's ratio of the tip layer on the interfacial stress distribution and the normal displacement on the top surface of the tip layer of the segmented composite structure is shown in Fig. A2.

Appendix B. A circular layer in axisymmetric condition

A circular layer (i.e. axisymmetric case) shown in Fig. B1 is examined and the results are compared with the plane strain case in the main manuscript. The elastic properties and boundary conditions are the same as those in the plane strain case. $U(r)$ in axisymmetric condition can be expressed as:

$$\begin{aligned} U_z\left(\frac{r}{R}\right) &= \sum_{i=0}^{n} a_i \cdot \delta_z^i\left(\frac{r}{R}\right) \\ U_r\left(\frac{r}{R}\right) &= 0 \end{aligned} \tag{B1}$$

The optimization framework is the same as that for plane strain case, except the squared deviation in axisymmetric case is calculated by:

$$\mathrm{Dev}(\sigma_{zz}) = \frac{1}{\pi R^2}\int_{r=0}^{R}\left(\sigma_{zz}-\sigma_{zz-avg}\right)^2\cdot 2\pi r\cdot dr \tag{B2}$$

Since the form of the stress distribution within the stress singularity dominated region is the same for both plane strain condition and axisymmetric condition (Khaderi et al., 2015), the squared deviation in axisymmetric condition in the stress singularity dominated region can be calculated by:

$$\frac{1}{\pi R^2}\int_{r=R-\varepsilon}^{R}\left(H(R-r)^{-0.41}-1\right)^2\cdot 2\pi r\cdot dr = \frac{1}{R^2}\left[\frac{100}{531}\varepsilon^{0.18}H^2(59R-9\varepsilon)+\frac{400}{9381}\varepsilon^{0.59}H(59\varepsilon-159R)-\varepsilon(\varepsilon-2R)\right] \tag{B3}$$

which is also bounded. For any λ in the range (-0.5, 0], the squared deviation in axisymmetric condition is bounded.

The numerical method is almost the same as the method used in plane strain cases, except axisymmetric quadrilateral elements (CAX4RH) were used to mesh the axisymmetric cases. The optimal results for a circular layer with $t/R = 0.1$ are summarized in Fig. B2.

Appendix C. Minimize the squared deviation without constraint $\underline{H} = 0$

The optimal results corresponding to the minimum squared deviation without constraint $H = 0$ for a flat layer with $t/L = 0.1$ are summarized in Fig. C1. The minimum squared deviation decreases and the normal stress distribution becomes more uniform as n increases, but the normal stress near the edge is still high. To highlight the normal stress distribution within the stress singularity dominated region near the edge, the normal stress is replotted in Fig. C1(c) on a logarithmic scale. From Fig. C1(c), it is clear that a lower minimum squared deviation obtained from a larger n does not help to reduce the stress within the stress singularity dominated region. The delamination may still initiate from the edge due to presence of high stress concentration.

Appendix D. Results for different t/L as a function of the order of polynomial series

The results corresponding to the minimum squared deviation under the constraint $H = 0$ for various n and different t/L are shown in Figs. D1 and 2. For $t/L = 0.05$, the minimum squared deviation reduces as n increases and reaches a plateau at $n = 10$ as shown in Fig. D1(a). For $t/L = 0.2$ and 0.4, the minimum squared deviation also decreases, reaching a plateau at $n = 4$ for $t/L = 0.2$ and $n = 2$ for $t/L = 0.4$, and then continue to reduce when $n > 5$ for $t/L = 0.2$ and $n > 3$ for $t/L = 0.4$. The cases corresponding to n lying in the first plateau in Fig. D1(a) are considered the *practical optimum cases* for all the t/L studied ($n = 10$ for $t/L = 0.05$ in Fig. D1(b), $n = 5$ for $t/L = 0.2$ in Fig. D1(c) and $n = 3$ for $t/L = 0.4$ in Fig. D1(d)).

Although an increase in n beyond the first plateau in Fig. D1(a) further reduces the minimum squared deviation ($n > 13$ for $t/L = 0.1$, $n > 5$ for $t/L = 0.2$, $n > 3$ for $t/L = 0.4$; n investigated in this study is not large enough for $t/L = 0.05$ to further reduce), the normal displacement applied near the edge changes from compression to tension and the magnitude of the tensile displacement increases as n increases (Fig. D2). For the case of $t/L = 0.4$ and $n = 7$, where the maximum normal stress observed is smaller than that of the practical optimum case, its maximum normalized tensile displacement applied at the edge is 26.4. Similarly, for the case of $t/L = 0.2$ and $n = 10$, the maximum normalized tensile displacement applied at the edge is 21.7. The requirement for such large displacements makes those normal displacement distributions impractical.

Appendix E. Analysis of the adhesion strength based on linear elastic fracture mechanics

In real scenarios, the interface is not perfectly bonded, and there are crack-like defects. The adhesion strength of an interface is determined by size of the defect and the local stress at the defect.

Linear elastic fracture mechanics is assumed. Consider an internal crack-like defect of radius a_{in}, which is assumed to be much smaller than the width of the tip layer $2L$. The stress σ_{in} at an internal crack (i.e. away from the edge) is related to the energy release rate as (Yao, 2013):

$$\sigma_{in} = \sqrt{\frac{\pi}{2}}a_{in}^{-0.5}\sqrt{GE^*} \tag{E1}$$

where G is the energy release rate and $E^*=E/(1-\nu^2)$. Define f as the ratio of the stress level σ_{in} at the crack position to the average stress σ_{avg}:

$$f = \frac{\sigma_{in}}{\sigma_{avg}} \tag{E2}$$

According to Griffith criterion ($G = G_c$), the failure strength due to this internal crack is:

$$\sigma_{in-c} = \frac{1.25}{f} a_{in}^{-0.5} \sqrt{G_c E^*} \tag{E3}$$

Assuming the size of the crack a_{in} is the same over the internal region of the contact, the internal position with highest stress level (i.e. highest f) will have the lowest failure strength among all internal cracks. Due to presence of a stress concentration and potential fabrication defects near the edge, the interface can also fail from an edge crack. Assuming the size of the edge crack a_{edge} is much smaller than the width of the tip layer $2L$, and is embedded in the stress singularity dominated region near the edge. The failure strength due to an edge crack can be calculated by (Balijepalli et al., 2017):

$$\sigma_{edge-c} = 0.39 \frac{1}{k} a_{edge}^{-0.094} L^{-0.406} \sqrt{G_c E^*} \tag{E4}$$

where k is a dimensionless calibration coefficient that depends on the design of the adhesive, and are found through obtaining intercept of the linear region in logarithmic plot Fig. 5(e) for different designs (Balijepalli et al., 2017).

Whether the interface fails from an internal crack or an edge crack is determined by which one has lower failure strength:

$$\frac{\sigma_{edge-c}}{\sigma_{in-c}} = 0.31 \frac{f_{\max}}{k} \frac{a_{in}^{0.5}}{a_{edge}^{0.094} L^{0.406}} \tag{E5}$$

If $\sigma_{edge\text{-}c}/\sigma_{in\text{-}c}>1$, the interface will fail from an internal crack; If $\sigma_{edge\text{-}c}/\sigma_{in\text{-}c}<1$, the interface will fail from an edge crack. Generally, we expect $a_{edge}>a_{in}$ due to fabrication defect at the edge, but as the exponent of a_{edge} is small, here we make a conservative estimate and assume $a_{edge}=a_{in}$. Eq. (E5) can then be expressed as:

$$\frac{\sigma_{edge-c}}{\sigma_{in-c}} = 0.31 \frac{f_{\max}}{k} \left(\frac{a_{in}}{L}\right)^{0.406}. \tag{E6}$$

Fig. E1(a) shows $\sigma_{edge\text{-}c}/\sigma_{in\text{-}c}$ for mushroom-shaped structures and composite structures as a function of a_{in}/L. Since $\sigma_{edge\text{-}c}/\sigma_{in\text{-}c}$ is a monotonic function of a_{in}/L, an edge crack failure is more favorable for small crack size a_{in}/L.

Since the practical optimum case has no stress concentration near the edge, it is expected to fail from an internal crack, and the adhesion strength can be calculated by Eq. (E3). Adhesion strength of those designs and their relative adhesion compared to the practical optimum case ($\sigma_c/\sigma_{opt\text{-}c}$) as a function of a_{in}/L are summarized in Fig. E1(b) and (c). Complete investigations of the adhesion strength and the transition of the crack initiation position from the edge to internal sites for mushroom-shaped structures and composite structures can be found in Benvidi and Bacca (2021) and Zhang et al. (2021).

Appendix F. Understanding of the segmented composite structure design with an elastic foundation model

The compressive displacement applied to the tip layer near the edge can be understood qualitatively by treating the tip layer as an elastic foundation. The elastic foundation has a spring stiffness $k = E^*/t$ and is bonded to a stiff edge plate with width $l = L\text{-}L_i$ near the edge as shown in Fig. F1(a). When the segmented composite structure is loaded by a remote tensile displacement y_0, the center of the tip layer is displaced uniformly by y_0 by the stiff center stalk, which results in an interfacial stress of ky_0 in the center. As the center of the tip layer is displaced by y_0, the inner end of the stiff edge plate is also displaced by y_0. Consider the stiff edge plate as rigid compared to the tip layer, the displacement of the edge plate varies linearly as:

$$y = ax + y_0. \tag{F1}$$

Moment equilibrium requires:

$$\int_0^l kyxdx = \int_0^l k(ax + y_0)xdx = 0, \tag{F2}$$

From which we can solve $a = -3y_0/2l$, and the displacement and stress is:

$$y = -\frac{3y_0}{2l}x + y_0, \tag{F3}$$

$$\sigma_{zz} = k\left(-\frac{3y_0}{2l}x + y_0\right). \tag{F4}$$

Eq. (F3) suggests that when $x>2/3l$, the displacement applied to the tip layer is compressive, which explains the presence of a compressive displacement near the edge in the segmented composite structure design. Note that the elastic foundation model is a one-dimensional model and does not take into account the lateral stresses and strains in the tip layer, which are significant for a nearly incompressible tip layer ($\nu = 0.49$). Thus it only provides a qualitative understanding on the mechanism of the design. A comparison between the prediction of the elastic foundation model and results from FE that simulates the segmented composite structure with a zero Poisson's ratio ($\nu = 0$) tip layer (which minimize the lateral deformation of the tip) is shown in Fig. F1(b) and (c), and there is reasonable agreement which justifies the mechanism proposed by the elastic foundation model.

Appendix G. Effect of the key dimensions of the segmented composite structure in axisymmetric condition

The effect of the center stalk radius and edge plate thickness of a circular segmented composite structure in axisymmetric condition on the interfacial normal stress distribution and the normal displacement applied on the top surface of the tip layer is summarized in Fig. G1.

A. *segmented composite structure with a recessed center stalk in axisymmetric condition*

The effect of w and m of the segmented composite structure with a recessed center stalk in axisymmetric condition is also studied and summarized in Fig. G2.

References

Akisanya, A.R., Fleck, N.A., 1997. Interfacial cracking from the free-edge of a long bi-material strip. Int. J. Solids Struct. 34, 1645–1665. https://doi.org/10.1016/S0020-7683(96)00053-4.

Aksak, B., Hui, C.Y., Sitti, M., 2011. The effect of aspect ratio on adhesion and stiffness for soft elastic fibres. J. R. Soc. Interface 8, 1166–1175. https://doi.org/10.1098/rsif.2010.0582.

Aksak, B., Murphy, M.P., Sitti, M., 2008. Gecko inspired micro-fibrillar adhesives for wall climbing robots on micro/nanoscale rough surfaces. In: Proceedings of the IEEE International Conference on Robotics and Automation, pp. 3058–3063. https://doi.org/10.1109/ROBOT.2008.4543675.

Aksak, B., Sahin, K., Sitti, M., 2014. The optimal shape of elastomer mushroom-like fibers for high and robust adhesion. Beilstein J. Nanotechnol. 5, 630–638. https://doi.org/10.3762/bjnano.5.74.

Anderson, T.L., 2005. Fracture Mechanics: Fundamentals and Applications, 3rd ed. Taylor & Francis, Boca Rotan, Florida. https://doi.org/10.1520/stp18822s. Metallurgia Italiana.

Anscombe, N., 2010. Direct laser writing. Nat. Photonics 4, 22–23. https://doi.org/10.1038/nphoton.2009.250.

Bacca, M., Booth, J.A., Turner, K.L., McMeeking, R.M., 2016. Load sharing in bioinspired fibrillar adhesives with backing layer interactions and interfacial misalignment. J. Mech. Phys. Solids 96, 428–444. https://doi.org/10.1016/j.jmps.2016.04.008.

Balijepalli, R.G., Begley, M.R., Fleck, N.A., McMeeking, R.M., Arzt, E., 2016. Numerical simulation of the edge stress singularity and the adhesion strength for compliant mushroom fibrils adhered to rigid substrates. Int. J. Solids Struct. 85–86, 160–171. https://doi.org/10.1016/j.ijsolstr.2016.02.018.

Balijepalli, R.G., Fischer, S.C.L., Hensel, R., McMeeking, R.M., Arzt, E., 2017. Numerical study of adhesion enhancement by composite fibrils with soft tip layers. J. Mech. Phys. Solids 99, 357–378. https://doi.org/10.1016/j.jmps.2016.11.017.

Bartlett, M.D., Croll, A.B., King, D.R., Paret, B.M., Irschick, D.J., Crosby, A.J., 2012. Looking beyond fibrillar features to scale gecko-like adhesion. Adv. Mater. 24, 1078–1083. https://doi.org/10.1002/adma.201104191.

F.H. Benvidi, M. Bacca, 2021. Theoretical limits in detachment strength for axisymmetric bi-material adhesives. arXiv Prepr. arXiv:2102.11324.

Carbone, G., Pierro, E., 2012. Sticky bio-inspired micropillars: finding the best shape. Small 8, 1449–1454. https://doi.org/10.1002/smll.201102021.

Carbone, G., Pierro, E., Gorb, S.N., 2011. Origin of the superior adhesive performance of mushroom-shaped microstructured surfaces. Soft Matter 7, 5545–5552. https://doi.org/10.1039/c0sm01482f.

Carlson, A., Kim-Lee, H.J., Wu, J., Elvikis, P., Cheng, H., Kovalsky, A., Elgan, S., Yu, Q., Ferreira, P.M., Huang, Y., Turner, K.T., Rogers, J.A., 2011. Shear-enhanced adhesiveless transfer printing for use in deterministic materials assembly. Appl. Phys. Lett. 98, 264104 https://doi.org/10.1063/1.3605558.

Carlson, A., Wang, S., Elvikis, P., Ferreira, P.M., Huang, Y., Rogers, J.A., 2012. Active, programmable elastomeric surfaces with tunable adhesion for deterministic assembly by transfer printing. Adv. Funct. Mater. 22, 4476–4484. https://doi.org/10.1002/adfm.201201023.

Del Campo, A., Greiner, C., Arzt, E., 2007. Contact shape controls adhesion of bioinspired fibrillar surfaces. Langmuir 23, 10235–10243. https://doi.org/10.1021/la7010502.

Drotlef, D.M., Amjadi, M., Yunusa, M., Sitti, M., 2017. Bioinspired composite microfibers for skin adhesion and signal amplification of wearable sensors. Adv. Mater. 29, 1–8. https://doi.org/10.1002/adma.201701353.

Fischer, S.C.L., Arzt, E., Hensel, R., 2017. Composite pillars with a tunable interface for adhesion to rough substrates. ACS Appl. Mater. Interfaces 9, 1036–1044. https://doi.org/10.1021/acsami.6b11642.

Fleck, N.A., Khaderi, S.N., McMeeking, R.M., Arzt, E., 2017. Cohesive detachment of an elastic pillar from a dissimilar substrate. J. Mech. Phys. Solids 101, 30–43. https://doi.org/10.1016/j.jmps.2017.01.001.

Gao, H., Chen, S., 2005. Flaw tolerance in a thin strip under tension. J. Appl. Mech. Trans. ASME 72, 732–737. https://doi.org/10.1115/1.1988348.

Gao, H., Wang, X., Yao, H., Gorb, S., Arzt, E., 2005. Mechanics of hierarchical adhesion structures of geckos. Mech. Mater. 37, 275–285. https://doi.org/10.1016/j.mechmat.2004.03.008.

Gao, H., Yao, H., 2004. Shape insensitive optimal adhesion of nanoscale fibrillar structures. Proc. Natl. Acad. Sci. USA. 101, 7851–7856. https://doi.org/10.1073/pnas.0400757101.

Gorb, S.N., Varenberg, M., 2007. Mushroom-shaped geometry of contact elements in biological adhesive systems. J. Adhes. Sci. Technol. 21, 1175–1183. https://doi.org/10.1163/156856107782328317.

Hawkes, E.W., Jiang, H., Christensen, D.L., Han, A.K., Cutkosky, M.R., 2018. Grasping without squeezing: design and modeling of shear-activated grippers. IEEE Trans. Robot. 34, 303–316. https://doi.org/10.1109/TRO.2017.2776312.

Hensel, R., Moh, K., Arzt, E., 2018. Engineering micropatterned dry adhesives: from contact theory to handling applications. Adv. Funct. Mater. 28, 1800865 https://doi.org/10.1002/adfm.201800865.

Howell, L.L., Magleby, S.P., Olsen, B.M., 2013. Handbook of Compliant Mechanisms. John Wiley & Sons Ltd.. Handbook of Compliant Mechanisms.

Hsu, Y.Y., Lucas, K., Davis, D., Elolampi, B., Ghaffari, R., Rafferty, C., Dowling, K., 2013. Novel strain relief design for multilayer thin film stretchable interconnects. IEEE Trans. Electron Devices 60, 2338–2345. https://doi.org/10.1109/TED.2013.2264217.

Hutchinson, J.W., Suo, Z., 1991. Mixed mode cracking in layered materials. Adv. Appl. Mech. https://doi.org/10.1016/S0065-2156(08)70164-9.

Jiang, Y., Grierson, D.S., Turner, K.T., 2014. Flat punch adhesion: transition from fracture-based to strength-limited pull-off. J. Phys. D Appl. Phys. 47, 325301 https://doi.org/10.1088/0022-3727/47/32/325301.

Johnston, I.D., McCluskey, D.K., Tan, C.K.L., Tracey, M.C., 2014. Mechanical characterization of bulk Sylgard 184 for microfluidics and microengineering. J. Micromech. Microeng. 24, 1–7. https://doi.org/10.1088/0960-1317/24/3/035017.

Khaderi, S.N., Fleck, N.A., Arzt, E., McMeeking, R.M., 2015. Detachment of an adhered micropillar from a dissimilar substrate. J. Mech. Phys. Solids 75, 159–183. https://doi.org/10.1016/j.jmps.2014.11.004.

Khungura, H., Bacca, M., 2021. Optimal load sharing in bioinspired fibrillar adhesives: asymptotic solution. J. Appl. Mech. Trans. ASME 88, 031004. https://doi.org/10.1115/1.4047859.

Kim-Lee, H.J., Carlson, A., Grierson, D.S., Rogers, J.A., Turner, K.T., 2014. Interface mechanics of adhesiveless microtransfer printing processes. J. Appl. Phys. 115, 104066 https://doi.org/10.1063/1.4870873.

Kim, S., Carlson, A., Cheng, H., Lee, S., Park, J.K., Huang, Y., Rogers, J.A., 2012. Enhanced adhesion with pedestal-shaped elastomeric stamps for transfer printing. Appl. Phys. Lett. 100, 171909 https://doi.org/10.1063/1.4706257.
Kim, S., Sitti, M., 2006. Biologically inspired polymer microfibers with spatulate tips as repeatable fibrillar adhesives. Appl. Phys. Lett. 89, 261911 https://doi.org/10.1063/1.2424442.
Kim, S., Sitti, M., Hui, C.Y., Long, R., Jagota, A., 2007. Effect of backing layer thickness on adhesion of single-level elastomer fiber arrays. Appl. Phys. Lett. 91, 161905 https://doi.org/10.1063/1.2801371.
Kim, T.K., Kim, J.K., Jeong, O.C., 2011. Measurement of nonlinear mechanical properties of PDMS elastomer. Microelectron. Eng. 1982–1985. https://doi.org/10.1016/j.mee.2010.12.108.
Kim, Y., Yang, C., Kim, Y., Gu, G.X., Ryu, S., 2020. Designing an adhesive pillar shape with deep learning-based optimization. ACS Appl. Mater. Interfaces 12, 24458–24465. https://doi.org/10.1021/acsami.0c04123.
King, D.R., Bartlett, M.D., Gilman, C.A., Irschick, D.J., Crosby, A.J., 2014. Creating gecko-like adhesives for "real world" surfaces. Adv. Mater. 26, 4345–4351. https://doi.org/10.1002/adma.201306259.
Long, R., Hui, C.Y., Kim, S., Sitti, M., 2008. Modeling the soft backing layer thickness effect on adhesion of elastic microfiber arrays. J. Appl. Phys. 104, 044301 https://doi.org/10.1063/1.2968249.
Luo, A., Mohammadi Nasab, A., Tatari, M., Chen, S., Shan, W., Turner, K.T., 2020. Adhesion of flat-ended pillars with non-circular contacts. Soft Matter 16, 9534–9542. https://doi.org/10.1039/d0sm01105c.
Luo, A., Turner, K.T., 2020. Mechanics of crack path selection in microtransfer printing: challenges and opportunities for process control. J. Mech. Phys. Solids 143, 104066. https://doi.org/10.1016/j.jmps.2020.104066.
Meitl, M.A., Zhu, Z.T., Kumar, V., Lee, K.J., Feng, X., Huang, Y.Y., Adesida, I., Nuzzo, R.G., Rogers, J.A., 2006. Transfer printing by kinetic control of adhesion to an elastomeric stamp. pdf Nat. Mater. 5, 33–38.
Menon, C., Murphy, M., Sitti, M., 2004. Gecko inspired surface climbing robots. In: Proceedings of the IEEE International Conference Robotics Biomimetics, IEEE ROBIO, 2004, pp. 431–436. https://doi.org/10.1109/robio.2004.1521817.
Micciché, M., Arzt, E., Kroner, E., 2014. Single macroscopic pillars as model system for bioinspired adhesives: Influence of tip dimension, aspect ratio, and tilt angle. ACS Appl. Mater. Interfaces 6, 7076–7083. https://doi.org/10.1021/am405873j.
Minsky, H.K., Turner, K.T., 2017. Composite microposts with high dry adhesion strength. ACS Appl. Mater. Interfaces 9, 18322–18327. https://doi.org/10.1021/acsami.7b01491.
Minsky, H.K., Turner, K.T., 2015. Achieving enhanced and tunable adhesion via composite posts. Appl. Phys. Lett. 106, 201604 https://doi.org/10.1063/1.4921423.
Murphy, M.P., Aksak, B., Sitti, M., 2009. Gecko-inspired directional and controllable adhesion. Small 5, 170–175. https://doi.org/10.1002/smll.200801161.
Pope, M.T., Kimes, C.W., Jiang, H., Hawkes, E.W., Estrada, M.A., Kerst, C.F., Roderick, W.R.T., Han, A.K., Christensen, D.L., Cutkosky, M.R., 2017. A multimodal robot for perching and climbing on vertical outdoor surfaces. IEEE Trans. Robot. 33, 38–48. https://doi.org/10.1109/TRO.2016.2623346.
Ranzani, T., Gerboni, G., Cianchetti, M., Menciassi, A., 2015. A bioinspired soft manipulator for minimally invasive surgery. Bioinspir. Biomim. 10, 1–14. https://doi.org/10.1088/1748-3190/10/3/035008.
Salonitis, K., 2014. Stereolithography. Comprehensive Materials Processing. Elsevier, pp. 19–67. https://doi.org/10.1016/B978-0-08-096532-1.01001-3.
Schneider, F., Fellner, T., Wilde, J., Wallrabe, U., 2008. Mechanical properties of silicones for MEMS. J. Micromech. Microeng. 1–9. https://doi.org/10.1088/0960-1317/18/6/065008.
Seghir, R., Arscott, S., 2015. Extended PDMS stiffness range for flexible systems. Sens. Actuators A Phys. 230, 33–39. https://doi.org/10.1016/j.sna.2015.04.011.
Sen, P., Xiong, Y., Zhang, Q., Park, S., You, W., Ade, H., Kudenov, M.W., O'Connor, B.T., 2018. Shear-enhanced transfer printing of conducting polymer thin films. ACS Appl. Mater. Interfaces 10, 31560–31567. https://doi.org/10.1021/acsami.8b09968.
Smith, R.S.H., Bader, C., Sharma, S., Kolb, D., Tang, T.C., Hosny, A., Moser, F., Weaver, J.C., Voigt, C.A., Oxman, N., 2020. Hybrid living materials: digital design and fabrication of 3D multimaterial structures with programmable biohybrid surfaces. Adv. Funct. Mater. 30, 1907401 https://doi.org/10.1002/adfm.201907401.
Song, S., Drotlef, Di.M., Majidi, C., Sitti, M., 2017. Controllable load sharing for soft adhesive interfaces on three-dimensional surfaces. Proc. Natl. Acad. Sci. USA. 114, E4344–E4353. https://doi.org/10.1073/pnas.1620344114.
Song, S., Sitti, M., 2014. Soft grippers using micro-fibrillar adhesives for transfer printing. Adv. Mater. 26, 4901–4906. https://doi.org/10.1002/adma.201400630.
Surjadi, J.U., Gao, L., Du, H., Li, X., Xiong, X., Fang, N.X., Lu, Y., 2019. Mechanical metamaterials and their engineering applications. Adv. Eng. Mater. 21, 1–37. https://doi.org/10.1002/adem.201800864.
Swallowe, G.M., Lee, S.F., 2006. Quasi-static and dynamic compressive behaviour of poly(methyl methacrylate) and polystyrene at temperatures from 293 K to 363 K. J. Mater. Sci. 41, 6280–6289. https://doi.org/10.1007/s10853-006-0506-9.
Tan, D., Luo, A., Wang, X., Shi, Z., Lei, Y., Steinhart, M., Kovalev, A., Gorb, S.N., Turner, K.T., Xue, L., 2020. Humidity-modulated core-shell nanopillars for enhancement of gecko-inspired adhesion. ACS Appl. Nano Mater. 3, 3596–3603. https://doi.org/10.1021/acsanm.0c00314.
Tang, T., Hui, C.Y., Glassmaker, N.J., 2005. Can a fibrillar interface be stronger and tougher than a non-fibrillar one? J. R. Soc. Interface 2, 505–516. https://doi.org/10.1098/rsif.2005.0070.
Tatari, M., Mohammadi Nasab, A., Turner, K.T., Shan, W., 2018. Dynamically tunable dry adhesion via subsurface stiffness modulation. Adv. Mater. Interfaces 5, 1800321. https://doi.org/10.1002/admi.201800321.
Thiel, M., Hermatschweiler, M., 2011. Three-dimensional laser lithography. Opt. Photonik 6, 36–39. https://doi.org/10.1002/opph.201190386.
Yao, H., 2013. Mechanics of robust adhesion of smooth biological attachment pads on rough surfaces. J. Adhes. Sci. Technol. 27, 775–782. https://doi.org/10.1080/01694243.2012.727151.
Yu, X., Zhou, J., Liang, H., Jiang, Z., Wu, L., 2018. Mechanical metamaterials associated with stiffness, rigidity and compressibility: a brief review. Prog. Mater. Sci. 94, 114–173. https://doi.org/10.1016/j.pmatsci.2017.12.003.
Zhang, X., Wang, Y., Hensel, R., Arzt, E., 2021. A design strategy for mushroom-shaped microfibrils with optimized dry adhesion: experiments and finite element analyses. J. Appl. Mech. 88, 031015 https://doi.org/10.1115/1.4049183.
Zhou, M., Tian, Y., Sameoto, D., Zhang, X., Meng, Y., Wen, S., 2013. Controllable interfacial adhesion applied to transfer light and fragile objects by using gecko inspired mushroom-shaped pillar surface. ACS Appl. Mater. Interfaces 5, 10137–10144. https://doi.org/10.1021/am402815x.